HEALTH AND MEDICINE

Bacteriocin-transport–inspired oral peptide-probiotic delivery ameliorates IBD complications via autophagy and gut homeostasis

Yang Yu[1,2]†, Yuting Bu[3]†, Chao Shen[1,4], Bingru Lin[3], Chao Lu[3], Lin Zhu[5], Zhe Shen[3]*, Chong Li[2]*, Xin Li[1,4]*

Copyright © 2026 The Authors, some rights reserved; exclusive licensee American Association for the Advancement of Science. No claim to original U.S. Government Works. Distributed under a Creative Commons Attribution NonCommercial License 4.0 (CC BY-NC).

Intestinal fibrosis (IF), a severe complication of inflammatory bowel disease (IBD), remains a critical unmet clinical need. Although the LL37 peptide and probiotics demonstrate therapeutic potential against IF, their clinical translation is hampered by enzymatic hydrolysis and rapid clearance. Here, inspired by the strategy of bacteriocin transport by bacteria (BTB), we developed an orally administered biotherapeutic platform [BTB–alginate (Alg)] featuring an "all-in-one" architecture that enables spatiotemporal coordination of LL37 and probiotics. The BTB-Alg effectively restored intestinal homeostasis through inflammation resolution, immune modulation, and gut microbiota reconstitution. Notably, integrated multiomics analysis and molecular dynamics simulations revealed that LL37 exerts antifibrotic effects by inducing adenosine 5′-monophosphate–activated protein kinase/mammalian target of rapamycin–mediated autophagy, a mechanism validated in clinical specimens. BTB-Alg exhibited potent therapeutic efficacy in three murine models of acute colitis, IBD-associated IF, and *Clostridioides difficile*–complicated colitis, highlighting its potential as an IBD treatment paradigm. This study offers a clinically translatable strategy for broad gastrointestinal applications.

INTRODUCTION

Intestinal fibrosis (IF), a progressive condition leading to intestinal dysfunction, is the most common complication (occurring in more than 50% of patients) of inflammatory bowel disease (IBD) (*1*). With the global incidence of IBD rising sharply, effective IF management has become an urgent unmet clinical need (*2*). Current therapies including mesalamine, corticosteroids, immunosuppressants, and biological agents show limited efficacy in halting fibrogenesis despite achieving inflammatory control (*3*). Fibrosis-induced obstruction necessitates multiple surgical interventions, with consequent short bowel syndrome and surgical complications, seriously impairing quality of life and survival rates (*4*).

The pathogenesis of IF involves the excessive deposition of extracellular matrix (ECM), secreted by pathological terminal effector cells (intestinal myofibroblasts), which are arise from intestinal fibroblasts by stimuli from a dysregulated intestinal microenvironment, comprising inflammatory cell infiltration, immune disturbances, and microbial dysbiosis (*5*). Consequently, single-target intervention often fails to address multifactorial nature of IF, causing the limited efficacy. We therefore propose that effective intervention requires simultaneous modulation of myofibroblasts and restoration of intestinal microenvironment homeostasis—a dual strategy targeting both effector cells and pathogenic drivers. In addition, this disrupted microenvironment creates favorable conditions for the colonization and overgrowth of *Clostridium difficile*, an opportunistic pathogen that recurs in more than 20% of patients with IBD. The toxins produced by *C. difficile* (TcdA and TcdB) further damage the intestinal epithelial barrier and exacerbate inflammatory responses, forming a vicious cycle that critically worsens the clinical course of IBD (*6*). Vancomycin (VAN) remains a standard therapeutic agent in clinical settings, but its efficacy is increasingly challenged by antibiotic resistance and the exacerbation of gut microbiota dysbiosis (*7*).

LL37, a 37–amino acid cathelicidin-derived antimicrobial peptide, demonstrates potent anti-inflammatory and immunomodulatory properties (*8*). Previous studies have found that LL37 notably alleviates symptoms of dextran sulfate sodium (DSS)–induced acute colitis (AC) and DSS/Crohn's disease (CD) dual-stimulation model colitis via enema (*9*–*11*). LL37 exhibits strong inhibitory effects on aberrant intestinal fibroblast activation, via mechanisms not fully delineated (*12*). These findings position LL37 as an extremely promising therapeutic candidate for IBD and its complications. Nevertheless, exploration of LL37 in IBD remains limited because of the unresolved challenge of oral targeted delivery to the distal gastrointestinal (GI) tract.

The biomimetic approach has been exploited in drug delivery by emulating natural biological phenomena. Bacteriocins are antimicrobial proteins or peptides synthesized by bacteria, serving as key tools for intraspecific and interspecific competition (*13*, *14*). At the specified time and location, bacteriocins are strategically synthesized and released in spatial coordination with bacterial colonization to exert their effects. This natural biological phenomenon forms a simple and efficient strategy of bacteriocin transport by bacteria (BTB) to the targeted sites. Therefore, inspired by the BTB strategy, we propose leveraging probiotics (functioning as both carriers and therapeutic agents) to deliver the LL37 (antimicrobial peptide) to specific sites. We engineered a biohybrid complex, referred to as BTB in this study, which integrates LL37 and probiotics. This approach minimizes the complexity of the drug delivery system while

[1]Department of Clinical Pharmacy, The First Affiliated Hospital, Zhejiang University School of Medicine, Hangzhou 310003, China. [2]College of Pharmaceutical Sciences, Southwest University, Chongqing 400715, China. [3]Department of Gastroenterology, The First Affiliated Hospital, Zhejiang University School of Medicine, Hangzhou 310003, China. [4]Zhejiang Provincial Key Laboratory for Drug Evaluation and Clinical Research, The First Affiliated Hospital, Zhejiang University School of Medicine, Hangzhou 310003, China. [5]School of Chinese Medicine, Hong Kong Baptist University, Hong Kong 999077, China.
*Corresponding author. Email: shenzdr@zju.edu.cn (Z.S.); chongli2009@gmail.com (C.L.); 11219017@zju.edu.cn (X.L.)
†These authors contributed equally to this work.

achieving a synergistic effect between the two therapeutic agents. This BTB recapitulates the natural "all-in-one" functional architecture to achieve synchronized LL37 delivery and microenvironment-responsive release (*15*). Besides, accumulating clinical evidence has established the pivotal role of probiotics in maintaining intestinal homeostasis, orchestrating mucosal immunity, and reinforcing epithelial barrier integrity (table S1) (*16*–*18*). Therefore, the BTB not only integrates the probiotics and bioactive peptide structurally but also maximizes dual effects of both LL37 and probiotics, acting on both effector cells and gut microenvironment, enhancing synergistic effects.

In this work, we developed BTB as a paradigm of structural and functional by biomimicry of bacterial behaviors. To further increase the efficiency of oral delivery of BTB, the biocomplex was encapsulated within a protective sodium alginate (Alg) shell. The BTB-Alg therapeutics was fabricated through sequential prebinding of positively charged LL37-decorated probiotics [*Lactobacillus* (Lac)] and negatively charged Alg, creating a probiotic-peptide–carrying symbiosis. Through bioinspired design, the BTB-Alg achieves precision integration of probiotics with LL37, enabling enhanced delivery of bioactive payloads with spatiotemporal control over component activation. In vivo, BTB extends intestinal residence of the probiotic-peptide combo while enabling targeted LL37 release and promoting probiotic colonization. Through integrated pharmacoengineering and multiomics approaches, we demonstrated that BTB-Alg restores intestinal homeostasis by simultaneously modulating inflammation, oxidative stress, immune activation, and gut microbiota composition. In murine models, this system exhibited superior efficacy in IF, AC, and dual-challenge colitis. We identified an adenosine 5′-monophosphate–activated protein kinase (AMPK)–dependent autophagy pathway, elucidating the antifibrotic mechanism of LL37 (Fig. 1). This BTB-Alg represents a considerable translational potential, offering a clinically implementable platform for IBD and related complication management.

RESULTS

Characterization of LL37 in vitro

To determine the optimal administered dosage and oral safety, we initially assessed the antifibrotic efficacy and cytotoxicity of LL37 in vitro (Fig. 2A). As showed in Fig. 2 (B to D) at a therapeutic concentration of 1.11 μM, LL37 substantially suppressed mRNA expression level of key fibrotic markers on transforming growth factor–β (TGF-β)–stimulated CCD-18Co cells, α–smooth muscle actin (α-SMA) by 41.85%, collagen type I alpha 1 (Col1α1) by 42.98%, and fibronectin (FN) by 89.83%. Furthermore, the protein expression levels of these fibrotic markers also decreased by LL37 (Fig. 2E). These results demonstrated that LL37 has potent inhibition of intestinal fibroblast activation and ECM secretion. The cytotoxicity assay showed that LL37 exhibited little toxicity at concentrations below 22.3 μM (80% survival rate), much higher than the effective concentration (1.11 μM), suggesting its oral safety (Fig. 2, F to H, and fig. S1). Subsequently, cellular affinity to intestinal myofibroblasts was assessed using Cyanine (Cy)5.5–labeled LL37. As Fig. 2 (I and J) and fig. S2 showed, compare with the quiescent intestinal fibroblasts, enhanced LL37 uptake was observed in TGF-β–treated CCD-18Co cells, which suggested an intrinsic targeting capability of LL37 toward pathological myofibroblasts within fibrotic niches. This preferential internalization by activated fibroblasts highlights its benefits in reducing nontargeted distribution in vivo. Besides, in the LL37-treated group, the immunofluorescence intensity of α-SMA was decreased, further verified the inhibitory effect on fibroblast activation. Collectively, these findings underscore favorable safety profile, selective accumulation, and potent antifibrotic effects of LL37, positioning it as a promising therapeutic agent for IF.

Design, screen, and fabrication of BTB-Alg

To achieve the oral application, we assessed the GI stability of LL37. It was found that LL37 maintained structural integrity in simulated gastric acid (SGF; pH 1.2) but underwent marked degradation upon exposure to pepsin (Fig. 2K and fig. S3). Therefore, the ability to resist enzymatic degradation is a critical design consideration for oral delivery of LL37. The Alg layer in our design would form a dense, three-dimensional nanonetwork that physically shields encapsulated payloads from exogenous digestive enzymes and spatial colocalization of the BTB (Fig. 2L). As bacteria are immune to the bacteriocins they secrete, the inhibitory activity of LL37 against Lac was evaluated. There are negligible effects on bacterial growth and proliferation at concentrations below 890 μM of LL37 (Fig. 2N and fig. S4). To quantify loading capacity of positively charged LL37 onto negatively charged Lac [1.0×10^9 CFU (colony-forming units)], we incubated 1 ml of fluorescein isothiocyanate (FITC)–labeled LL37 solutions [at an LL37–equivalent (equiv.) concentration of 8.34, 16.7, 33.4, 66.8, 134, 223, 334, and 556 μM] with Lac to fabricate Lac/LL_{1-8} complexes (Fig. 2O). Fluorescence intensity analysis revealed progressive LL37 adsorption up to Lac/LL_6, beyond which saturation occurred (Fig. 2P and fig. S5A). Besides, the zeta potential was no more increase from Lac/LL_6 to Lac/LL_7, which confirmed the maximal LL37 deposition (Fig. 2Q). Quantitative analysis of unbound LL37 in the supernatants revealed loading efficiencies of 92.26% (Lac/LL_5), 85.30% (Lac/LL_6), and 59.81% (Lac/LL_7), demonstrating concentration-dependent encapsulation characteristics (Fig. 2R). Last, Lac/LL_6 (BTB), with 853 μg of LL37 deposited per 1×10^9 CFU of Lac, was selected for optimal LL37 utilization. Next, an anionic Alg layer was deposited onto the cationic BTB complex, with fluorescence intensity of precipitates increasing incrementally with Cy5.5-labeled Alg concentration (Fig. 2, S and T, and fig. S5B). To balance protective efficacy and bacterial division, we optimized coating density taking LL37 protection efficiency as a screening index. Lac/LL@Alg-2, Lac/LL@Alg-5, and Lac/LL@Alg-10 with different Alg density were incubated in SGF with pepsin for 2 hours, and then the residual LL37 on Lac was detected. Compared to Lac/LL@Alg-2, both Lac/LL@Alg-5 and Lac/LL@Alg-10 exhibited high residual LL37 ratios, with no significant difference (Fig. 2, U and V). These results indicate that the Alg layer in Lac/LL@Alg-5 could effectively prevent LL37 leakage and pepsin penetration. Consequently, Lac/LL@Alg-5 was selected for BTB-Alg subsequent studies.

Characterization of BTB-Alg

The integrated structure of BTB-Alg was systematically validated through physicochemical, structural, and functional analyses. Sequential layer deposition was confirmed via zeta potential shifts from -15.63 ± 1.2 mV (native Lac) to $+3.36 \pm 0.8$ mV after LL37 combing, followed by reversal to -9.33 ± 0.9 mV post–Alg encapsulation (Fig. 3A). Correspondingly, the average particle size of Lac/LL@Alg increased relative to that of Lac (Fig. 3, B and C). Confocal laser scanning microscopy (CLSM) with triple fluorescent labeling (FITC-Lac: green; Cy3-LL37: red; Cy5.5-Alg: purple) revealed precise spatial colocalization of all components, visualizing the Lac/

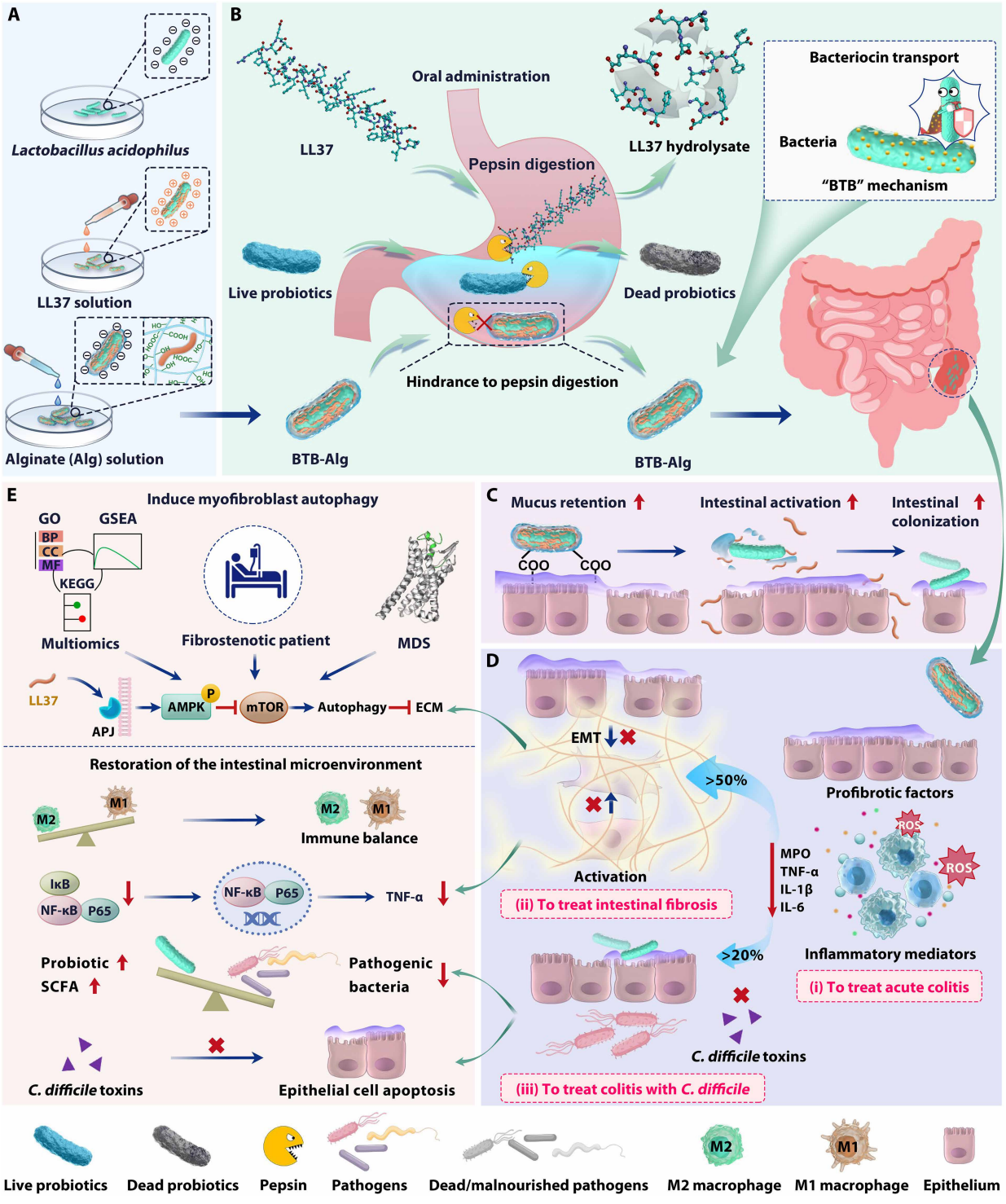


Fig. 1. Bioinspired construction of BTB-Alg for IBD therapy: Inflammation, fibrostenosis, and *C. difficile* infection. (**A**) Bioinspired design of BTB biocomposites. (**B**) Protective mechanisms of orally delivered probiotics and LL37 in the GI tract via microbial mimicry. (**C**) Following oral administration, BTB-Alg undergoes sequential intestinal adhesion, payload release, tissue penetration, and lesion-specific targeting. (**D**) BTB-Alg alleviates AC, resolves fibrosis, and suppresses *C. difficile* infection (CDI). (**E**) Mechanism of BTB-Alg–mediated intestinal niche reprogramming. ROS, reactive oxygen species; MDS, molecular dynamics simulation; SCFA, short-chain fatty acid; BP, biological process; CC, cellular component; MF, molecular function.

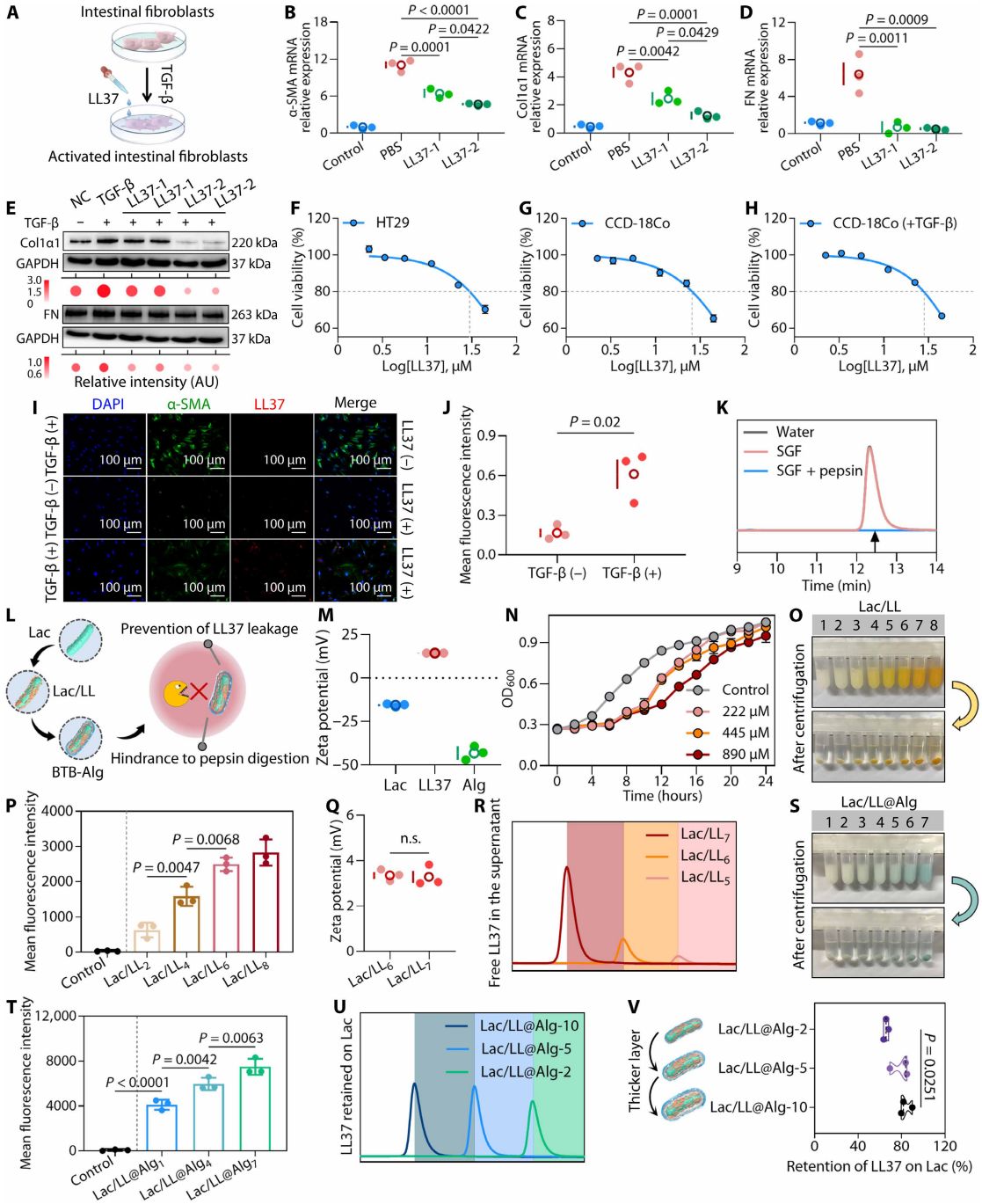


Fig. 2. In vitro characterization and systematic optimization of BTB-Alg. (**A** to **D**) Antifibrosis efficacy of LL37 by quantitative polymerase chain reaction (qPCR) analysis of fibrotic markers (α-SMA, Col1α1, and FN) in TGF-β–stimulated CCD-18Co cells treated with LL37-1 (1.11 μM) or LL37-2 (11.1 μM). (**E**) Western blot assays of Col1α1 and FN protein expression. AU, arbitrary units; NC, negative control. (**F** to **H**) Cytotoxicity assessment of LL37 in (F) HT29 cells, (G) unstimulated CCD-18Co cells, and (H) TGF-β–pretreated (24 hours) CCD-18Co cells. (**I** and **J**) Cellular uptake of Cy5.5-labeled LL37 (20 μg ml^{-1}) in unstimulated versus TGF-β–stimulated intestinal fibroblasts (I), with fluorescence intensity quantification (J). Scale bars, 100 μm. (**K**) Chromatogram profiles of LL37 detected by high-performance liquid chromatography (HPLC) following different treatments. (**L**) Fabrication schematic of BTB-Alg. (**M**) Zeta potential of Lac, LL37, and Alg. (**N**) Growth kinetics of Lac with LL37 coculture. (**O**) Fluorescence imaging of LL37 loading optimization [37.5, 75, 150, 300, 600, 1000, 1500, and 2500 μg of LL37 per 1×10^9 colony-forming units (CFU) of Lac]. (**P**) Fluorescence intensity of different BTB models. (**Q**) Zeta potential stabilization at saturation (Lac/LL_6 versus Lac/LL_7). n.s., not significant. (**R**) HPLC quantification of unbound LL37 in supernatants. (**S**) Alg coating optimization using Cy5.5-labeled Alg (0.032, 0.063, 0.125, 0.25, 0.5, 1, or 2 mg per 1×10^9 CFU of Lac). (**T**) Fluorescence intensity of Alg deposition. (**U** and **V**) Protective efficacy of Alg against pepsin degradation. HPLC chromatograms (U) and residual ratio of LL37 quantification (V). In (B) to (D), (F) to (H), (J), (M), (N), (P), (Q), (T), and (V), data are shown as mean ± SD (n = 3 biological replicates). Statistical analysis was performed via a one-way analysis of variance (ANOVA) or an unpaired Student's two-sided t test. Experiments in (E), (I), (K), (O), (R), (S), and (U) repeated three times with consistent results.

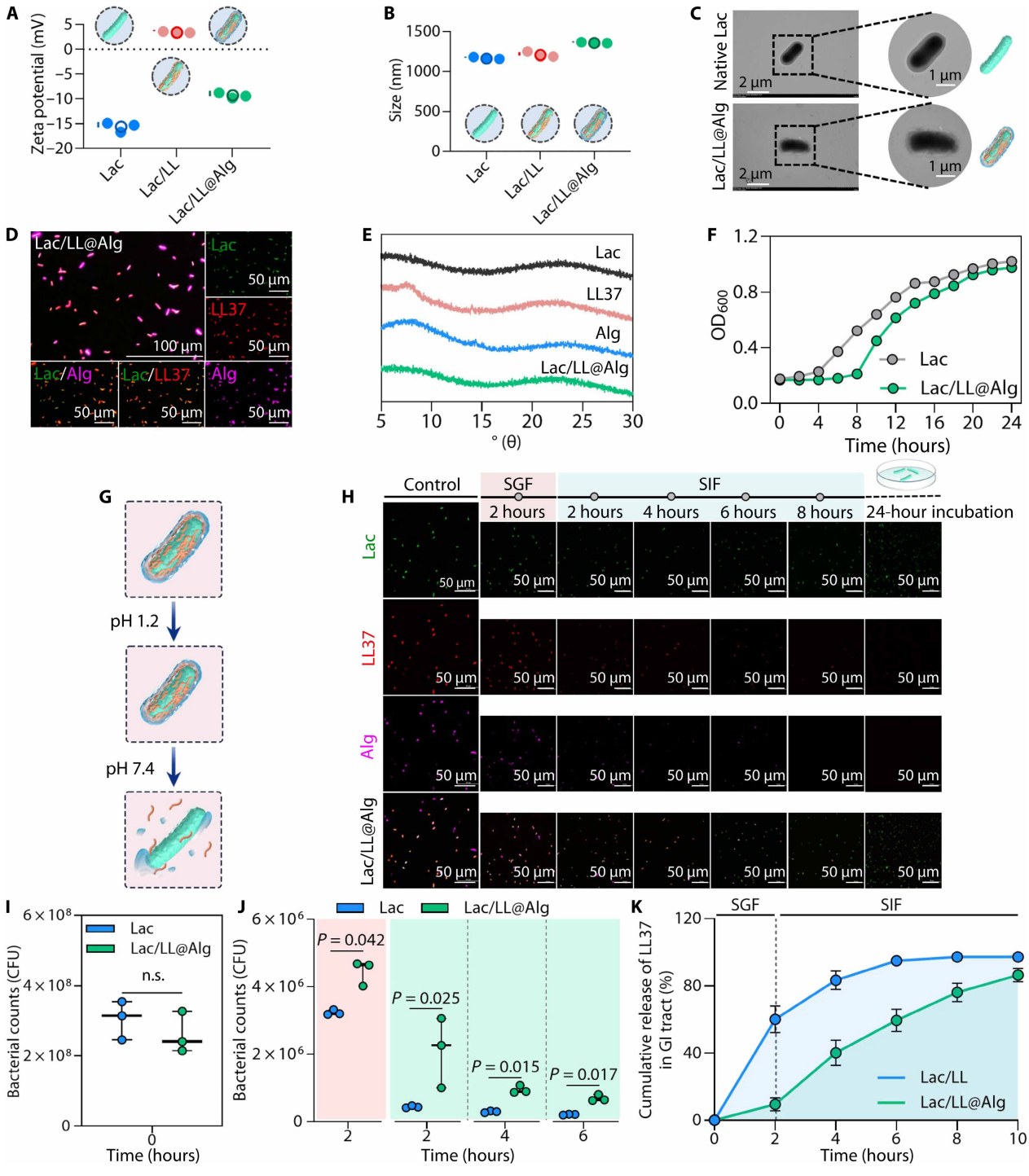


Fig. 3. Structural characterization, GI stability, and targeted release of BTB-Alg. (**A**) Surface charge evolution during the decoration. (**B** and **C**) Particle size (B) and transmission electron microscopy (TEM) images (C) showing structural transitions. Scale bars, 2 and 1 μm. (**D**) Triple-channel confocal imaging confirming core-shell architecture: FITC-labeled Lac [green; excitation/emission (Ex/Em): 490/520 nm], Cy3-labeled LL37 (red; Ex/Em: 550/570 nm), and Cy5-labeled Alg (purple; Ex/Em: 646/664 nm). Scale bars, 100 and 50 μm. (**E**) XRD patterns demonstrating LL37 crystalline structure attenuation after Alg encapsulation. (**F**) Growth curves of Lac and Lac/LL@Alg at 37°C recorded at 2-hour interval for 24 hours. (**G**) Schematic illustration of the physiological responsiveness behavior of Lac/LL@Alg. (**H**) Fluorescence images of Lac/LL@Alg after incubation with SGF supplemented with pepsin for 2 hours and SIF supplemented with pancreatin for 2, 4, 6, and 8 hours. FITC-labeled Lac (green), Cy3-labeled LL37 (red), and Cy5-labeled Alg (purple), respectively. Scale bar, 50 μm. (**I** and **J**) Survival of Lac and Lac/LL@Alg measured on the basis of plate counts after incubation with SGF supplemented with pepsin and SIF supplemented with pancreatin at 0 point (I) and indicated times (J). (**K**) Cumulative release profiles of LL37 from Lac/LL or Lac/LL@Alg after incubation with SGF and SIF. In (A), (B), (F), and (I) to (K), data are shown as mean ± SD (n = 3 biological replicates). Experiments in (C) to (E) and (H) repeated three times with consistent results.

LL@Alg architecture (Fig. 3D). X-ray diffraction (XRD) analysis showed the disappearance of characteristic peak of LL37 upon Alg coating, suggesting effective encapsulation and structural integration (Fig. 3E). Lac growth and division rates in Lac/LL@Alg were comparable to native Lac, demonstrating that the coating process had negligible effects on bacterial viability (Fig. 3F and fig. S6). Then, fluorescently labeled Lac/LL@Alg was used to detect the physiological separation of Alg layer, and CLSM images showed that LL37 and Alg colocalized with Lac during the initial 2 hours in SGF, demonstrating the integrity structure. Upon transfer to simulated intestinal fluid (SIF), gradual dissociation of Alg layer and LL37 release were observed, confirming pH-responsive payload delivery (Fig. 3, G and H). After incubation, Lac bacterial binary fission was found via CLSM, suggesting the viability of Lac in the Alg layer. Plate count assays quantitatively validated enhanced Lac survival in Lac/LL@Alg compared to native Lac after 2 hours in SGF supplemented with pepsin (Fig. 3, I and J, and fig. S7). Fluorescence tracking of Cy3-labeled LL37 revealed minimal release (<15%) in SGF, demonstrating the protective efficacy of Alg structure (Fig. 3K and fig. S8). In contrast, LL37 release in Lac/LL (without Alg layer) was faster, highlighting the critical role of the Alg layer. These results demonstrate that our BTB-Alg design ensures structural integrity, bioactive, and spatiotemporal codelivery of biotherapeutics.

BTB-Alg enhances intestinal retention and mucosal penetration in vivo

To evaluate the spatiotemporal retention of BTB-Alg, DSS-induced IF model mice received oral administrations of native Lac (FITC-labeled), free LL37 (Cy5.5-labeled), and Lac/LL@Alg [FITC-labeled Lac/Cy5.5-labeled LL37/indocyanine green (ICG)–labeled Alg] for real-time GI tract tracking (Fig. 4A and fig. S9). Fluorescence imaging revealed that the fluorescence intensities of both Lac and LL37 derived from Lac/LL@Alg were substantial higher than those of native Lac or free LL37 in vivo at 2, 4, 6 and 8 hours postadministration, indicating superior intestinal retention of BTB (Fig. 4, B to E). For BTB, the fluorescence signals of biological complex and Alg layer in Lac/LL@Alg were colocalized in the stomach at 2 hours initially. Upon reaching the intestinal tract, the signals progressive spatial dissociated, revealing a phase-specific behavior (Fig. 4D). By 8 hours, the Alg layer exhibited the most degradation, with a 79.33% reduction in fluorescence intensity, while Lac and LL37 retained 80.05 and 37.34% of their initial signals, respectively, demonstrating the gradual separation of the Alg layer and sustained retention of Lac and LL37 (Fig. 4F). These findings suggested successful Lac colonization and extended retention of LL37 in vivo. Besides, the BTB demonstrated pronounced mucosal adherence and permeation as the stronger fluorescence imaging in excised intestinal tissues (Fig. 4, G and H), showing 2.79- and 4.48-fold higher fluorescence intensities for Lac and LL37 components, respectively, compared to native Lac and free LL37 controls. The frozen sections of intestinal tissues also showed obvious colocalization and penetration of BTB (fig. S10).

Then, to detect in vivo diffusion dynamics of BTB-Alg in the mucus layer, we compared native Lac, free LL37, and Lac/LL@Alg penetration through ex vivo rat intestinal mucus. FITC-labeled Lac, Cy5.5-labeled LL37, and dual fluorescent–labeled Lac/LL@Alg were applied to a 2-cm mucus column and allowed to diffuse for 24 hours (Fig. 4I). Bottom-layer aliquots (50 μl) were collected at 8 and 24 hours for fluorescence quantification. Native Lac exhibited severely restricted mobility (<6% penetration at 8 hours), whereas free LL37 demonstrated rapid diffusion (>60% penetration within 8 hours) (Fig. 4, J and K). This divergence likely arises from electrostatic interactions, and the negatively charged mucus matrix repels anionic Lac but facilitates cationic LL37 transport through charge attraction. Lac/LL@Alg displayed intermediate penetration efficiency, achieving 16.23% Lac and 48.17% LL37 permeation at 24 hours, attributable to its balanced surface charge, hydrogen bonding, and polymer chain entanglement with mucus. Notably, the higher accumulation of LL37 relative to Lac in the bottom layer likely arises from the sustained release of LL37 during the diffusion process. Last, we validated the mucosal permeation of BTB-Alg using stenotic intestinal tissues from patients with CD. Following 4 hours of incubation with stenotic intestinal tissues, CLSM revealed substantial BTB-Alg infiltration (Fig. 4L), demonstrating the great biocompatibility and tissue-penetrating capacities. These findings collectively indicate that the BTB-Alg architecture realized integrated delivery and segmented decomposition behavior for probiotics and peptides.

BTB-Alg exhibits potent therapeutic efficacy for murine model of AC

We first assessed oral therapeutic efficacy of BTB-Alg in DSS-induced AC model (Fig. 5A). As showed in Fig. 5 (B and C), administration of the Lac/LL@Alg markedly attenuated disease progression, as evidenced by suppressed body weight loss and disease activity index (DAI) scores in mice during the study. Notably, Lac/LL@Alg treatment restored colon length, decreased the colonic weight-length index, and indicated morphological recovery (Fig. 5, D to F). Histopathological analysis revealed that Lac/LL@Alg ameliorated severe epithelial disruption, immune cell infiltration, and restored goblet cell populations, thus reducing histological scores of AC models (Fig. 5, G and H). Besides, Lac/LL@Alg reduced inflammation levels, as evidenced by the reduced spleen weight index, lower level of tumor necrosis factor–α (TNF-α), and higher level of interleukin-10 (IL-10) (Fig. 5, I to K). Compared to AC mice, oxidative stress damage was also reduced as evidenced by the decreased level of myeloperoxidase (MPO) and malondialdehyde (MDA; Fig. 5, L and M). Therefore, Lac/LL@Alg reduced inflammation and oxidative damage, repaired the intestinal mucosal epithelium, and maintained the intestinal mucosal barrier integrity in vivo.

Then, the intestinal floras homeostasis was detected by 16*S* ribosomal RNA (rRNA) sequencing analysis. It was found that Lac/LL@Alg restored balance of intestinal gut microbiota (Fig. 5, N and O). The community composition at the phylum and genus levels showed that the therapeutic intervention substantially increased the abundance of *Bacillota* (associated with anti-inflammatory effects) and reduced that of *Bacteroidota* (associated with inflammation and metabolic dysfunction), which are typically depleted and enriched in the IBD, respectively (Fig. 5P) (*19*, *20*). At the genus level, the increased abundance of two well-documented probiotics, *norank_f__Muribaculaceae* and *Ligilactobacillus*, contributed to gut immune modulation and enhanced mucosal barrier function, collectively supporting the alleviation of IBD (Fig. 5, Q and S) (*21*). Notably, enriched colonic Lac populations confirmed targeted probiotic delivery and colonization (Fig. 5R). Thus, the 16*S* rRNA sequencing analysis demonstrated effective restorement of gut microbiota homeostasis by BTB intervention in GI tracts.

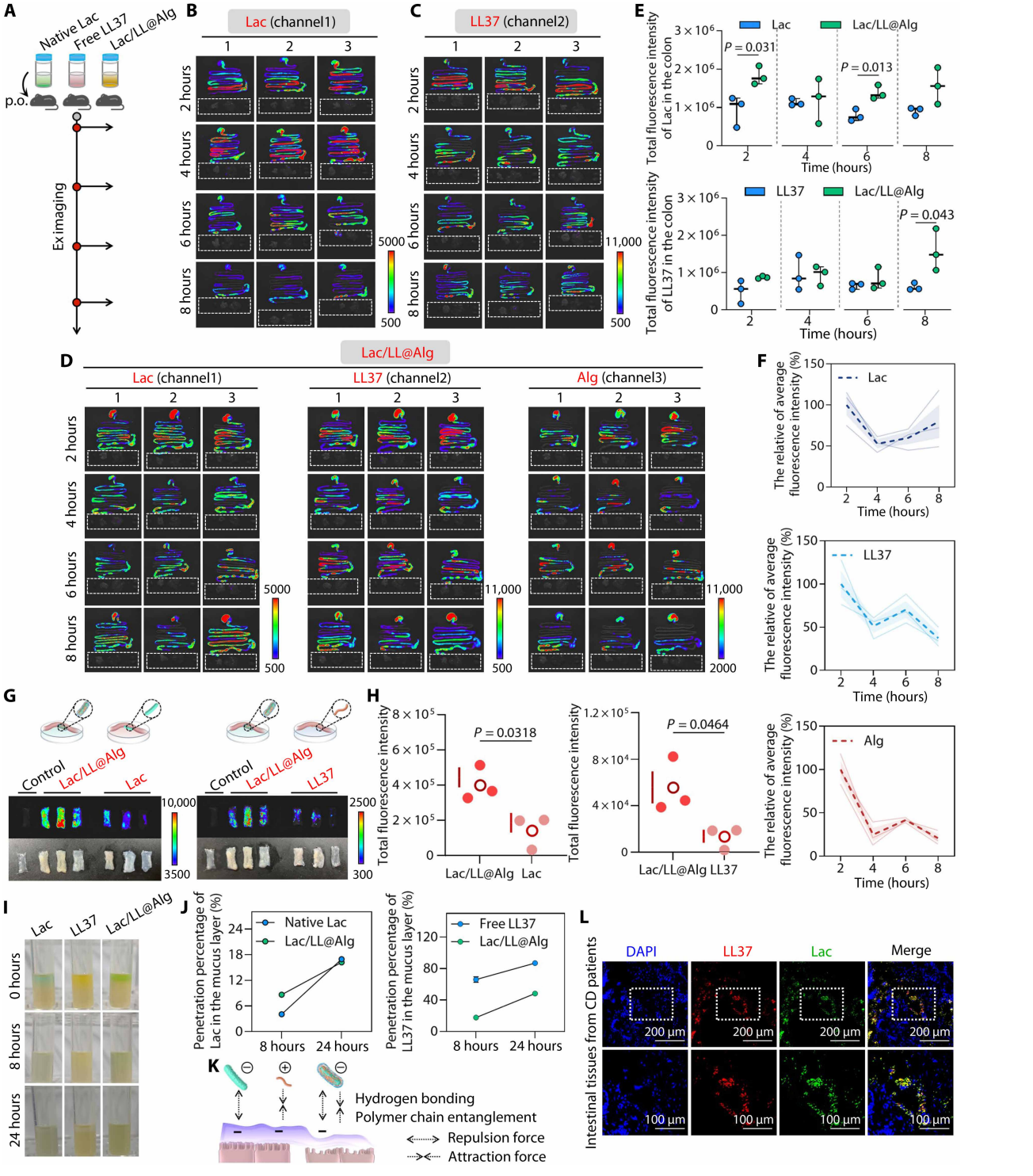


Fig. 4. In vivo GI retention and mucoadhesion profiling of BTB-Alg. (**A**) The workflow of in vivo tissue distribution experiments. p.o., per os. (**B** to **D**) IVIS imaging of the GI tract (top) and major organs (bottom) after oral administration of (B) FITC-labeled native Lac, (C) Cy5.5-labeled free LL37, and (D) triple-labeled Lac/LL@Alg at specified time points ($n = 3$). (**E**) The quantification of total colonic fluorescence intensity for Lac and LL37 over time. (**F**) Time-dependent fluorescence changes of Lac, LL37, and Alg components in Lac/LL@Alg at 2, 4, 6, and 8 hours postadministration. (**G** and **H**) Colonic mucosal retention analysis of (G) representative images and (H) quantification of total intensity of different groups after 8 hours postadministration ($n = 3$). (**I** to **K**) Representative images (I), penetration ratios (J), and a schematic diagram (K) demonstrate the effective diffusivity of Lac, LL37, and Lac/LL@Alg in mucus. (**L**) Effective penetration of Lac/LL@Alg in intestinal tissues derived from patients with CD. Data in (E), (F), (H), and (J) presented as mean ± SD ($n = 3$ biological replicates). Significance determined by unpaired two-tailed Student's *t* test. Experiments in (B) to (D), (G), (I), and (L) repeated three times with consistent results.

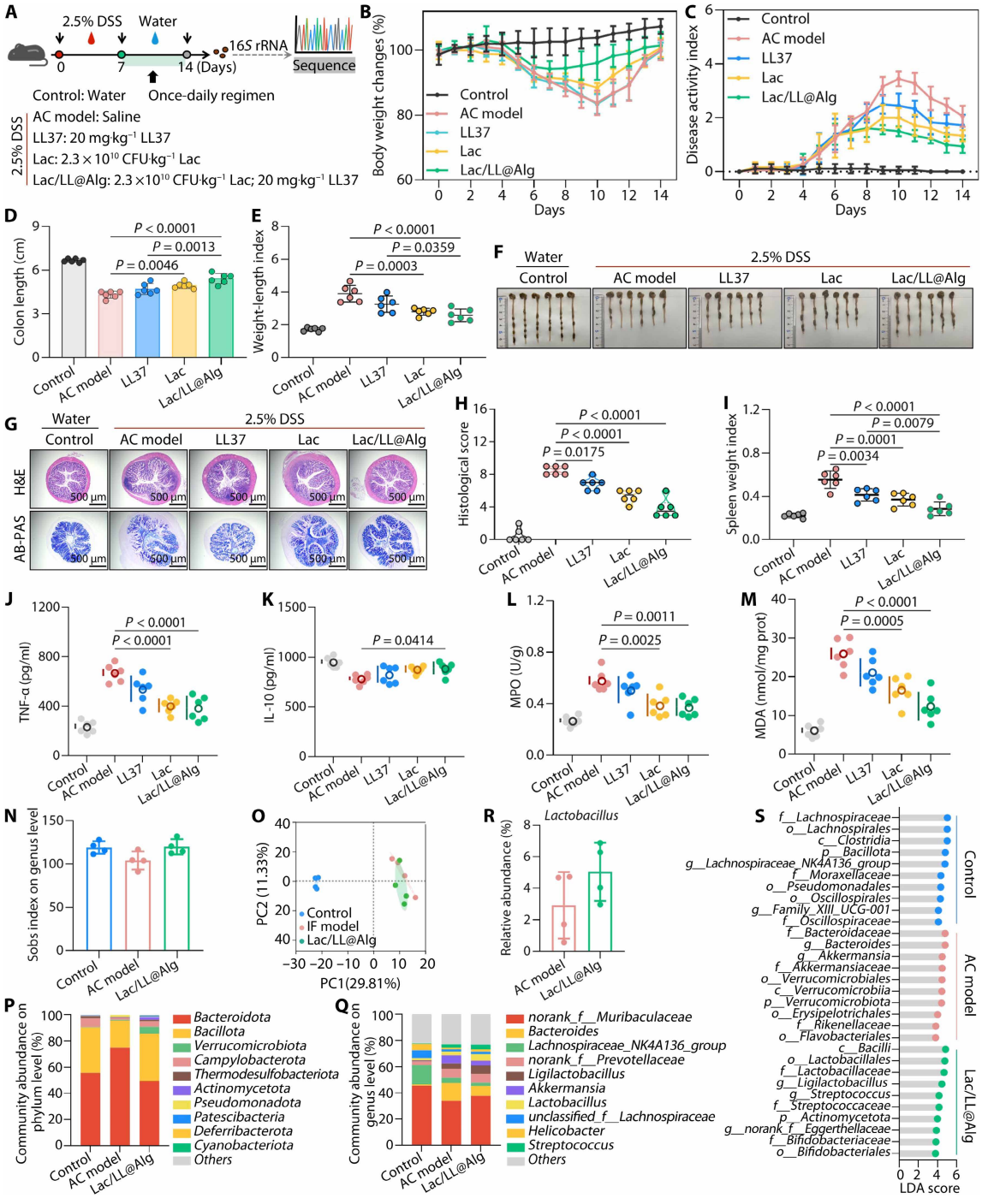


Fig. 5. Oral administration of BTB-Alg alleviates DSS-induced AC. (**A**) Schematic representation of DSS-induced AC in mice and therapeutic design. (**B**) Daily body weight changes throughout the study. (**C**) DAI changes during the whole study. (**D** to **F**) Colon length (D), weight length index (E), and morphology (F) across different groups. (**G**) Hematoxylin and eosin (H&E) and Alcian blue-periodic acid schiff (AB-PAS) staining of intestines from each group. Scale bars, 500 μm. (**H**) H&E-based histopathological scoring of colonic tissues posttreatment. (**I**) Spleen weight index in each group. (**J** to **M**) Measurement of TNF-α (J), IL-10 (K), MPO (L), and MDA (M) in different groups. prot, protein. (**N**) Analysis of Sobs index at the genus level. (**O**) Principal components analysis elucidated the similarity of gut microbial communities at the genus level. PC1, principal component 1. (**P** and **Q**) The composition of microbial communities was characterized at both phylum (P) and genus (Q) levels from the control, AC model, and Lac/LL@Alg. Bars represent relative abundance. (**R**) Relative abundance of Lac in feces from AC model and Lac/LL@Alg groups. (**S**) Linear discriminant analysis Effect Size (LEfSe) was implemented to identify differentially enriched taxa in gut microbiota among control, AC model, and Lac/LL@Alg-treated groups. Data in (B) to (M) are derived from $n = 6$ biological independent samples. In (B) to (E) and (H) to (M), data are shown as mean ± SD, with statistical analysis performed via one-way ANOVA. *P* values denote the statistical significance between AC model and LL37, Lac, and Lac/LL@Alg. In (N) to (S), data are shown as mean ± SD ($n = 4$ biological independent samples), with statistical analysis analyzed via one-way ANOVA or a Student's two-sided *t* test.

BTB-Alg exhibits potent therapeutic efficacy for murine model of dual-challenge colitis

Building on the therapeutic efficacy observed in the AC model, we further evaluated the BTB-Alg system on *C. difficile*–infected DSS-induced colitis, which was a serious infection complication of IBD in clinic. Mice model of colitis with *C. difficile* infection (CDI) was established as shown in Fig. 6A. It was found that *C. difficile* colonization required prior colitis induction, as evidenced by 25.90-fold higher fecal TcdB toxin levels in saline (DSS + CDI) group versus CD group (Fig. 6B). Besides, there is no significant difference in body change and inflammatory levels between control and CD groups (Fig. 6, C to I). Compared to DSS-induced colitis, saline (DSS + CDI)–treated mice exhibited aggravated disease severity, as evidenced by reduced survival, pronounced colon shortening, exacerbated weight loss, and elevated inflammatory markers (Fig. 6, C, D, and J to N). Notably, Lac/LL@Alg treatment demonstrated comprehensive therapeutic effects in the dual-challenge model, showing improved survival rate, marked attenuation of weight loss, and preservation of colon architecture (Fig. 6, C, D, O, and P, and fig. S11). At the molecular level, colonic IL-6, IL-17, and IL-1β mRNA levels were down-regulated by 75.99, 71.89, and 23.79%, compared to the saline-treated group (Fig. 6, Q to S). Besides, Lac/LL@Alg treatment pronounced enhanced intestinal barrier function, as indicated by increased zonula occludens-1 (ZO-1) expression (Fig. 6T and fig. S12). Histopathological analysis revealed complete epithelial preservation and intact crypt structures in Lac/LL@Alg-treated mice, contrasting with extensive ulceration and crypt abscesses in saline control (Fig. 6U). While VAN-treated mice maintained colon length (6.44 ± 0.26 cm versus 5.45 ± 0.19 cm in saline-treated group) and body weight (10.87% loss versus 16.52% in saline-treated group), it induced pronounced cecal dilation, indicative of antibiotic-associated dysbiosis. Mechanistically, the exacerbation of intestinal inflammation by CD infection primarily involves *C. difficile* toxin-mediated hyperactivation of the nuclear factor κB (NF-κB) signaling cascade and skewed macrophage polarization toward proinflammatory M1 phenotype (*11*). So, we further detected the effects of Lac/LL@Alg on these pathological processes. As can be seen in Fig. 6 (V and W), Lac/LL@Alg-treated group down-regulated the NF-κB pathway while promoting macrophage polarization from M1 phenotype toward M2 phenotype, thereby alleviating intestinal inflammation. The 16*S* rRNA sequencing analysis demonstrated that the BTB-Alg improves the gut microbiota homeostasis by improving the diversity and structure as showed in fig. S13, which demonstrated microbiota modulation as a key therapeutic mechanism for Lac/LL@Alg (*22*). In contrast, the gut microbiota homeostasis was serious damaged in the VAN-treated group, although improving the length of the colon.

BTB-Alg exhibits potent therapeutic efficacy for murine model of colitis-associated IF

Building on these findings, we systematically evaluated the therapeutic potential of BTB-Alg on chronic colitis-associated IF (Fig. 7A). In the DSS-induced colitis model, prolonged chronic inflammatory resulted in substantial decreased body weight, shortened colon length, and histopathological damage. Lac/LL@Alg administration resulted in the most weight recovery among all intervention groups (Fig. 7B). Morphometric analysis revealed that colons in the Lac/LL@Alg group were longer (5.73 ± 0.39 cm) than those in the IF model mice (4.68 ± 0.22 cm), free LL37–treated mice (5.18 ± 0.13 cm), or native Lac–treated mice (5.33 ± 0.16 cm) (Fig. 7, C and D). Histological examination demonstrated a marked reduction in IF-associated pathology in Lac/LL@Alg-treated mice, including decreased leukocyte infiltration and ECM deposition between submucosal and muscular layers compared to IF model (Fig. 7E and fig. S14). Quantitative histological and fibrosis scoring confirmed superior therapeutic outcomes in the Lac/LL@Alg group, with marked mitigation of both inflammatory progression and fibrotic remodeling relative to other treatments (Fig. 7, F and G). Specifically, Lac/LL@Alg administration reversed IF-induced up-regulation of Col I in the mucosal lamina propria and α-SMA thickening in smooth muscle layers (Fig. 7, H and I, and fig. S15) while suppressing fibrogenesis-related transcripts (α-SMA, Col1α1, and FN) at the mRNA level (Fig. 7, J to L, and fig. S16). Then, the colon tissues were collected and subjected to immunofluorescence staining to detect the epithelial-mesenchymal transition (EMT) process, a biological process (BP) in which epithelial cells lose their characteristic features and acquire mesenchymal traits (*23*). We found the intervention of Lac/LL@Alg blocked the EMT process, as evidenced by reduced vimentin expression in Lac/LL@Alg-treated mice compared to control group (Fig. 7M). Collectively, these results demonstrate that Lac/LL@Alg exerts multifaceted therapeutic effects in the IF model as mitigating intestinal inflammation, preserving mucosal barrier integrity, reducing ECM deposition, and showing no toxicity in vivo (fig. S17). Notably, BTB-Alg consistently demonstrated broad-spectrum therapeutic efficacy across AC, dual-challenge colitis, and IF, three IBD-related models, highlighting its potential as a versatile platform for clinical utility for IBD management.

BTB-Alg reshapes gut microbiota homeostasis

To elucidate the mechanistic basis of BTB-Alg–mediated intestinal homeostasis, we performed metagenomic sequencing on fecal samples from control, IF model, and Lac/LL@Alg-treated mice (Fig. 8A). A total of 5035 species was shared across groups with comparable α-diversity (Fig. 8, B and C, and fig. S18A). Principal coordinate analysis revealed distinct microbial community structures, indicating treatment-specific microbiome remodeling (Fig. 8D and fig. S18B). Lac/LL@Alg administration reversed fibrotic dysbiosis by restoring phylum-level equilibrium, increasing immunomodulatory *Bacillota* populations while normalizing *Verrucomicrobiota* abundance (Fig. 8, E to G, and fig. S18C) (*24*). Targeted enrichment of colonic Lac populations confirmed effective probiotic delivery and colonization (Fig. 8, F and G). Functional profiling via Kyoto Encyclopedia of Genes and Genomes (KEGG) analysis demonstrated pathological enrichment of profibrotic pathways (ECM synthesis, lipopolysaccharide biosynthesis, and inflammatory response) in IF models versus control (fig. S19) (*25*). In contrast, Lac/LL@Alg-treated mice down-regulated these profibrotic pathways and exhibited enhanced DNA repair mechanisms (nucleotide excision repair and mismatch repair), pathways critical for maintaining genomic stability (Fig. 8H) (*26*, *27*). Notably, an important metabolic regulation pathway—AMPK signaling—was up-regulated, suggesting the improved intestinal energy metabolism by Lac/LL@Alg (*28*). Subsequently, we assessed the homology between our metagenomic reads from the virulence factor database (VFDB) as the virulence factors that contribute to the fibrosis process with relative virulence factors of bacteria through inducing immune dysfunction (*29*). Concurrent reduction in microbial virulence factors further highlighted depletion of pathogenic bacteria and intestinal microenvironmental improvement (fig. S20). Overall, the functional composition in gut microbiome was recovered in Lac/LL@Alg-treated group compared

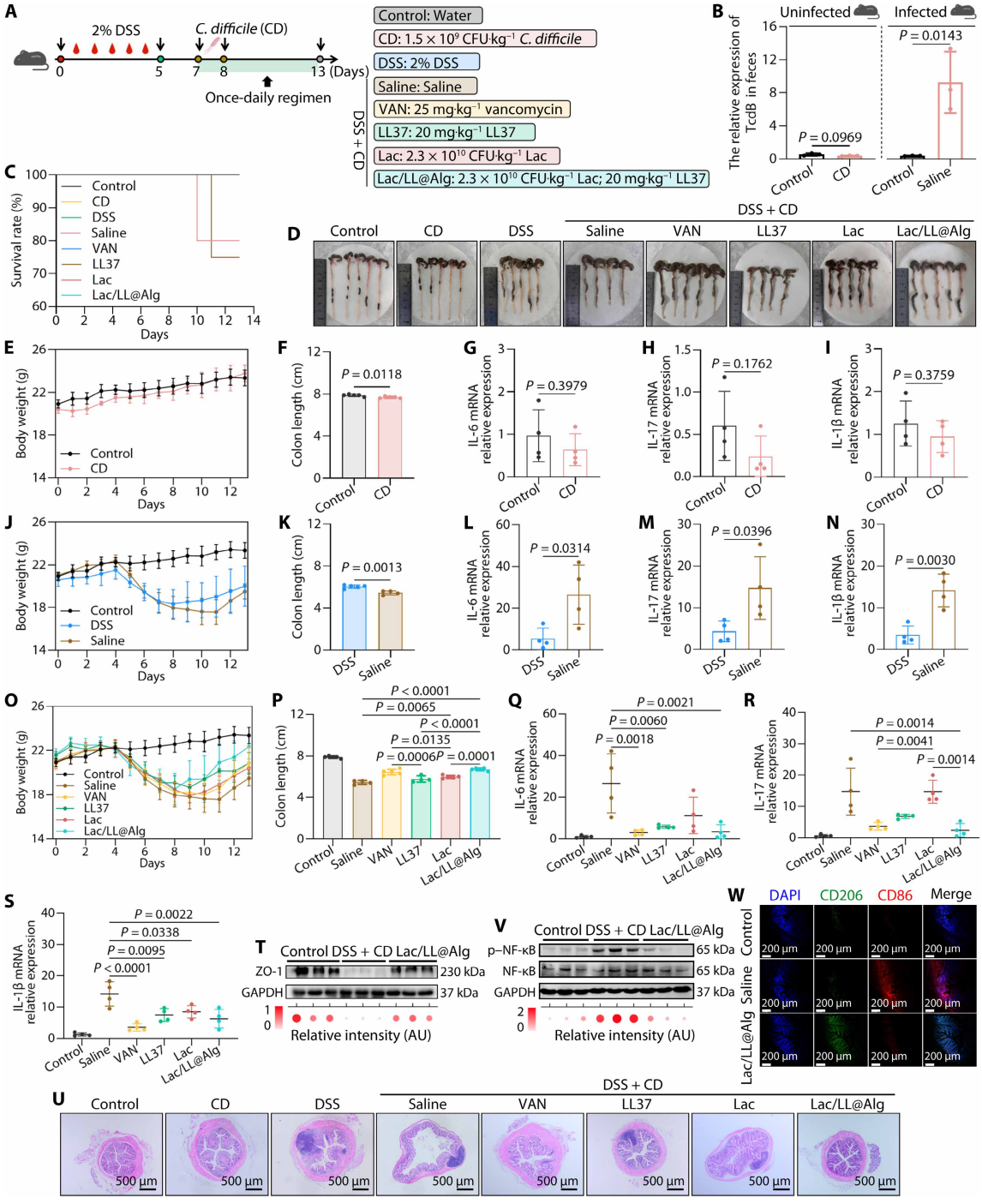


Fig. 6. Oral BTB-Alg alleviates DSS and *C. difficile*–induced colitis in mice. (**A**) Schematic representation of DSS and *C. difficile*–induced colitis in mice and therapeutic design. (**B**) TcdB expression in feces from control, CD, and saline (DSS + CD)–treated groups on day 8 ($n = 3$). (**C**) Survival curves of mice with different treatments. (**D**) Representative colon morphology images from different groups ($n = 5$). (**E** to **I**) Body weight changes (E), colon lengths (F), and proinflammatory markers [IL-6 (G), IL-17 (H), and IL-1β (I) mRNA levels] between control and CD-treated groups. (**J** to **N**) Body weight changes (J), colon lengths (K), and proinflammatory markers [IL-6 (L), IL-17 (M), and IL-1β (N) mRNA levels] between CD and saline-treated groups. (**O** to **S**) Body weight changes (O), colon lengths (P), and proinflammatory markers [IL-6 (Q), IL-17 (R), and IL-1β (S) mRNA levels] from different treatment groups. (**T**) Western blot analysis of ZO-1 expression in different treatment groups ($n = 3$). (**U**) H&E staining of intestinal tissues from each group ($n = 3$). Scale bars, 500 μm. (**V**) Western blot analysis of NF-κB pathway in different treatment groups ($n = 3$). p–NF-κB, phosphorylated NF-κB. (**W**) Immunofluorescence staining of macrophages with distinct phenotypes ($n = 3$). CD206 staining (green): M2 macrophage; CD86 staining (red): M1 macrophage. Scale bars, 200 μm. In (G) to (I) and (L) to (N), data are shown as mean ± SD ($n = 4$ biological replicates), with statistical analysis conducted via an unpaired Student's two-sided *t* test. In (Q) to (S), data are shown as mean ± SD ($n = 4$ biological replicates), with statistical analysis conducted via one-way ANOVA. *P* values denote the statistical significance among the saline, VAN, LL37, Lac, and Lac/LL@Alg groups.

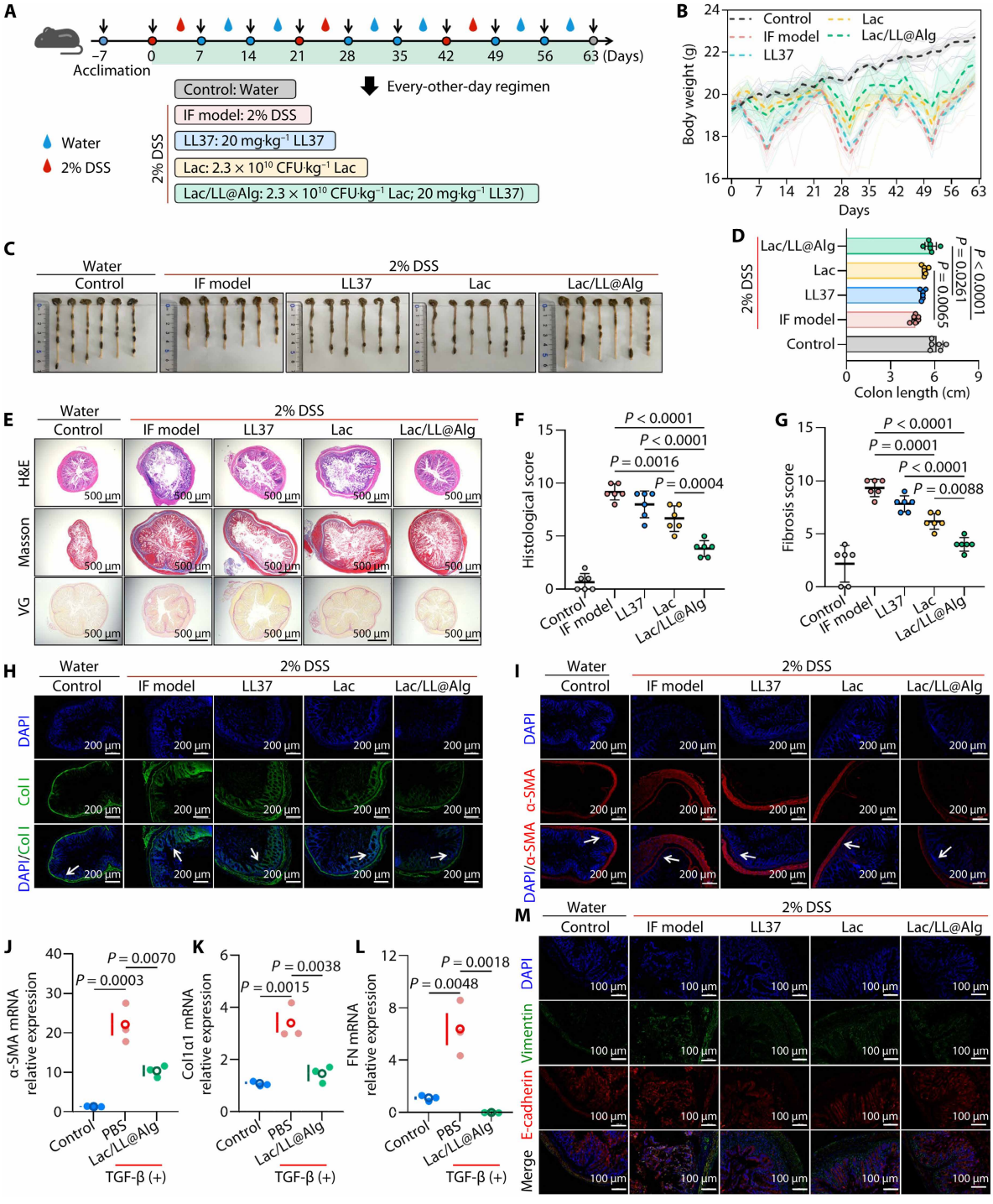


Fig. 7. Oral BTB-Alg alleviates DSS-induced IF. (**A**) Experimental design of DSS-induced IF model and the timeline of therapeutic intervention. (**B**) Body weight changes during whole treatment. (**C** and **D**) Colon morphology (C) and length quantification (D) in different groups. (**E**) Histopathological analysis via H&E, Masson's trichrome, and Van Gieson (VG) staining. Scale bars, 500 μm. (**F** and **G**) Quantitative histological scoring of inflammation (F) and fibrosis severity (G). (**H** and **I**) Immunofluorescence imaging of Col I (H) and α-SMA (I). Scale bars, 200 μm. (**J** to **L**) qPCR analysis of fibrotic markers α-SMA (J), Col1α1 (K), and FN (L) in CCD-18Co cells (C_{LL37} = 1.11 μM). (**M**) EMT modulation with vimentin (green) and E-cadherin (red) costaining. Scale bars, 100 μm. In (B), (D), (F), and (G), data are shown as mean ± SD (n = 6 biological replicates). In (J) to (L), data are shown as mean ± SD (n = 3 biological replicates). Statistical analysis was studied via one-way ANOVA, with P values denoting the statistical significance among the IF model, LL37, Lac, and Lac/LL@Alg groups. The images in (E), (H), (I), and (M) are representative of five biological replicates.

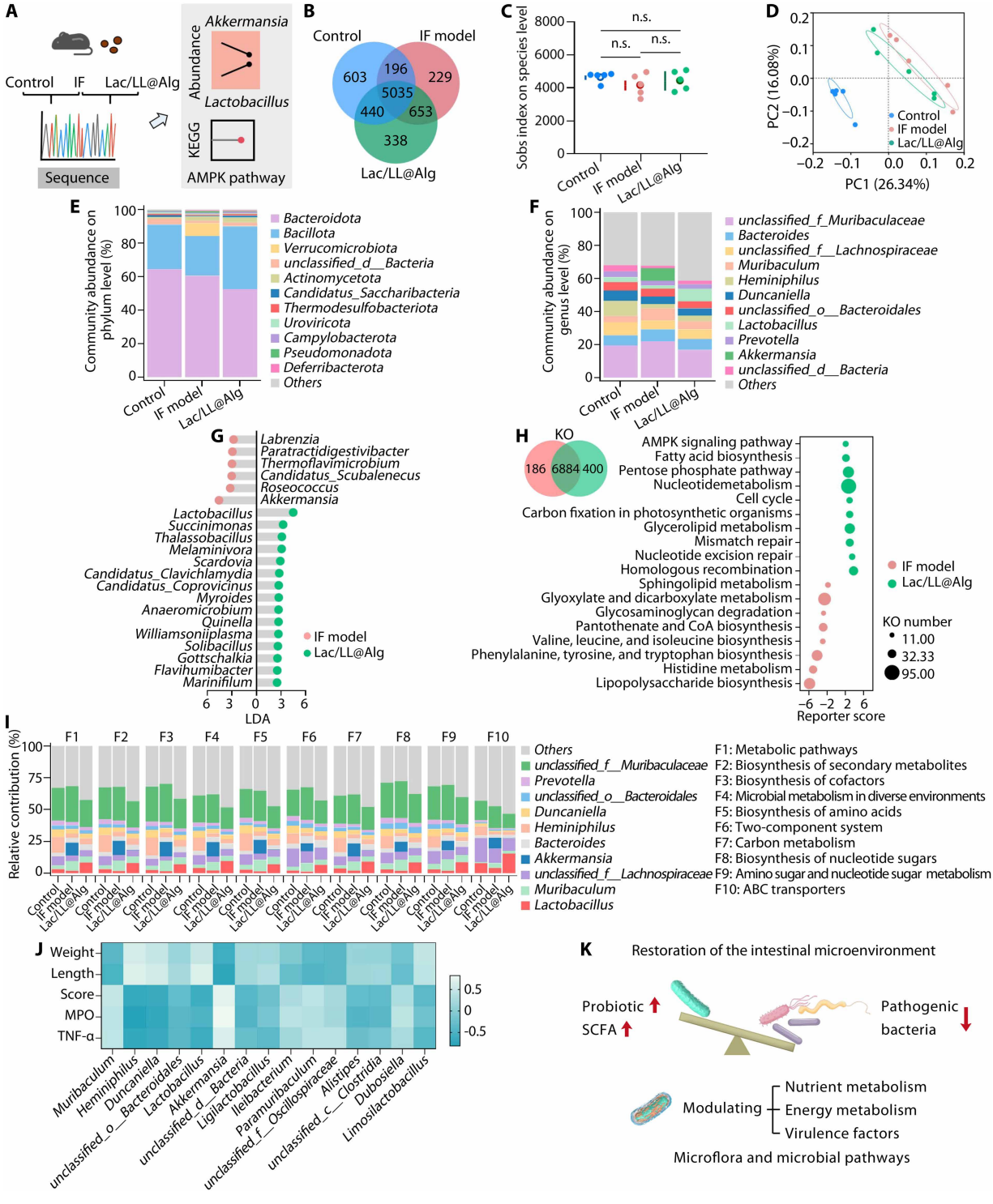


Fig. 8. Gut microbiome reconfiguration by BTB-Alg treatment. (**A**) The workflow for metagenomic analysis. (**B** and **C**) Evaluation of species-level diversity using Venn diagrams (B) and the Sobs index (C). (**D**) Principal coordinate analysis of microbial community structures. (**E** and **F**) Abundance profiles of microbial communities at the phylum (E) and genus (F) levels following different treatments. (**G**) LEfSe analysis identifying differentially abundant taxa between the IF model and Lac/LL@Alg groups [linear discriminant analysis (LDA) score > 2.5]. (**H**) KEGG pathway enrichment analysis for IF model versus Lac/LL@Alg. CoA, coenzyme A. KO, KEGG Orthology. (**I**) KEGG functional contribution degree in control, IF model, and Lac/LL@Alg groups at the genus level (top 10). ABC, adenosine 5′-triphosphate–binding cassette. (**J**) Correlation coefficients between differentially enriched microbes and IF-related parameters. (**K**) Proposed mechanism illustrating the microbiome-mediated therapeutic effects of BTB-Alg treatment. Data are shown as mean ± SD (n = 5 biological replicates). Statistical comparisons between control, IF model, and Lac/LL@Alg groups were studied via one-way ANOVA.

with that in IF model, and Lac played an important role in the functional relative contribution (Fig. 8I); this was consistent with the changes in microbial abundance. A Spearman correlation analysis established *Lactobacillus* abundance as positively associated with clinical improvement (body weight and colon length) and negatively correlated with fibrotic markers (fibrosis scoring, MPO, and TNF-α) (Fig. 8J). These findings collectively demonstrate that Lac/LL@Alg reprograms gut microbiota composition and functionality through suppression of profibrotic metabolic pathways, activation of host-protective DNA repair mechanisms, and systemic reduction of virulence and oxidative stress (*30*). This multilevel modulation substantiates the capacity of Lac/LL@Alg to break the pathogenic cycle of microbiota dysregulation and IF, as well as improving intestinal homeostasis (Fig. 8K).

BTB-Alg down-regulates the expression of fibrosis-related proteins

To delineate the protein-level mechanisms underlying the antifibrotic effects of BTB-Alg, we performed quantitative proteomics analysis of colon tissue across control, IF model, and Lac/LL@Alg-treated groups (Fig. 9A). A total of 8214 expressed proteins was identified across the groups, with no major differences in proteomic coverage (Fig. 9B). Principal components analysis revealed distinct proteomic signatures, confirming treatment-specific molecular remodeling (Fig. 9C). Differential expression analysis identified 1270 proteins dysregulated in the IF model compared to control, with 634 proteins modulated by Lac/LL@Alg intervention (Fig. 9D and fig. S21). Weighted gene coexpression network analysis further established phenotype-proteome correlations, providing mechanistic biomarkers for therapeutic evaluation (fig. S22, A and B, and table S2). Differentially expressed proteins (DEPs) underwent functional characterization through Gene Ontology (GO) term annotation and KEGG pathway enrichment analysis. Comparative profiling between the IF model and control or Lac/LL@Alg-treated groups revealed pronounced alterations across molecular functions, cellular components, and BPs (Fig. 9, E and F). Further analysis of BPs highlighted that the therapeutic effects of Lac/LL@Alg were closely linked to LL37 binding, with key pathway distinctions including immune regulation, metabolic reprogramming, and cytoskeletal remodeling (figs. S23 and S24). KEGG pathway and gene set enrichment analysis (GSEA) revealed substantial dysregulation of proteins in the IF model compared to control, with up-regulated pathways including leukocyte chemotaxis, cell adhesion, innate immune response, and ECM synthesis (Fig. 9, G and H, and fig. S25). As important upstream effector cells in IBD, macrophages drive chronic inflammation by orchestrating the initial antigen response and propagating inflammatory signals. Furthermore, M1 macrophages secrete profibrotic factors and activate fibroblasts, thereby driving aberrant ECM deposition (*31*, *32*). Elevated M1 macrophage infiltration was confirmed in the intestinal stricture tissue of patients with CD (Fig. 9I). In contrast, the Lac/LL@Alg treatment alleviates inflammatory responses and reduces immune cell infiltration while also reducing the polarization of M1 macrophages and down-regulating the fibrotic pathway (Fig. 9, K to N, and fig. S26) (*33*, *34*). Notably, proteomic analysis identified up-regulation of AMPK and apelin signaling pathways in Lac/LL@Alg-treated mice (Fig. 9, N and O). The AMPK pathway, a central metabolic regulator governing cell growth and apoptosis, was particularly noteworthy, as it emerged as pathway marked enriched in both proteomic and metagenomic analyses in BTB-Alg–treated group. Besides, given its established regulatory roles in cardiac and hepatic fibrotic pathologies, we further systematically investigate its specific role in IF resolution (*35*, *36*).

AMPK-mediated autophagic flux drives the antifibrotic action of LL37

We first examined the level of AMPK activation in stenotic tissues and healthy tissues from patients with CD, which revealed a marked decrease in AMPK activation levels in stenotic tissues (Fig. 10, A and B). Then, in TGF-β–stimulated CCD-18Co cells, we found that both free LL37 and Lac/LL@Alg notably activated the AMPK pathway while down-regulating fibrotic markers (Fig. 10, C to E). Furthermore, quantitative analysis revealed that AMPK phosphorylation was predominantly mediated by free LL37 (accounting for 95.83% of the total effect) and exhibited dose-dependent activation kinetics (Fig. 10D and fig. S27). Subsequently, using the AMPK agonist metformin (Met) as a positive control, the AMPK-mediated antifibrotic effects were further verified in CCD-18Co cells (*37*). As shown in Fig. 10 (F to H), the antifibrotic efficacy of LL37 (α-SMA reduction: 96.61%; Col I reduction: 99.50%; FN reduction: 53.36%) and Met was substantially attenuated by cotreatment with compound C (CC), an AMPK inhibitor (*38*). Collectively, these results demonstrate that AMPK activation is essential for LL37-mediated antifibrotic actions. Notably, Lac/LL@Alg exhibited greater resistance to CC-mediated inhibition (α-SMA reduction: 52.20%; Col I reduction: 70.91%; FN reduction: 36.94%) than free LL37, suggesting additional Lac-dependent protective mechanisms (Fig. 10, F to H).

We sought to delineate the downstream mediators underlying the antifibrotic effects of LL37-AMPK signaling. A cross-analysis integrating canonical AMPK functions (glucose metabolism, lipid oxidation, and autophagy), murine fibrosis model data, and gene expression profiles of patients with IBD from Gene Expression Omnibus datasets was conducted. This integrative analysis identified autophagy suppression as the predominant pathway in IF, consistent with reported evidence that impaired autophagic flux drives myofibroblast activation (Fig. 10I and figs. S28 and S29). Subsequently, the down-regulation of autophagy in stenotic tissues was validated at the clinical sample level (Fig. 10J). Ultimately, the autophagy-restoring capacity of LL37 was mechanistically demonstrated. Notably, compared to control, LL37 treatment robustly activated autophagy in intestinal fibroblasts, as evidenced by an increased LC3B-II/LC3B-I ratio, p62 degradation, and reduced mammalian target of rapamycin (mTOR) phosphorylation—key markers of autophagic flux (Fig. 10, K and L). Collectively, these findings demonstrate that LL37 alleviates colitis-associated fibrosis by enhancing autophagic flux via AMPK activation. Turning our attention to the apelin pathway, an upstream regulatory receptors of AMPK, was also enriched following Lac/LL@Alg treatment (Fig. 10M) (*39*). Given the established role as a G protein–coupled receptor (GPCR) ligand of LL37, we hypothesized direct binding between LL37 and the apelin receptor (APJ; a GPCR) as a trigger for AMPK activation. Molecular dynamics (MD) simulations confirmed strong LL37-APJ binding affinity, comparable to that of the endogenous ligand apelin-36 binding to APJ, which provides a structural basis for AMPK activation through GPCR signaling (Fig. 10, N to P, and fig. S30) (*40*). Therefore, BTB-Alg mitigates IF by inducing AMPK-dependent autophagy in intestinal fibroblasts, probably depending on LL37-APJ binding.

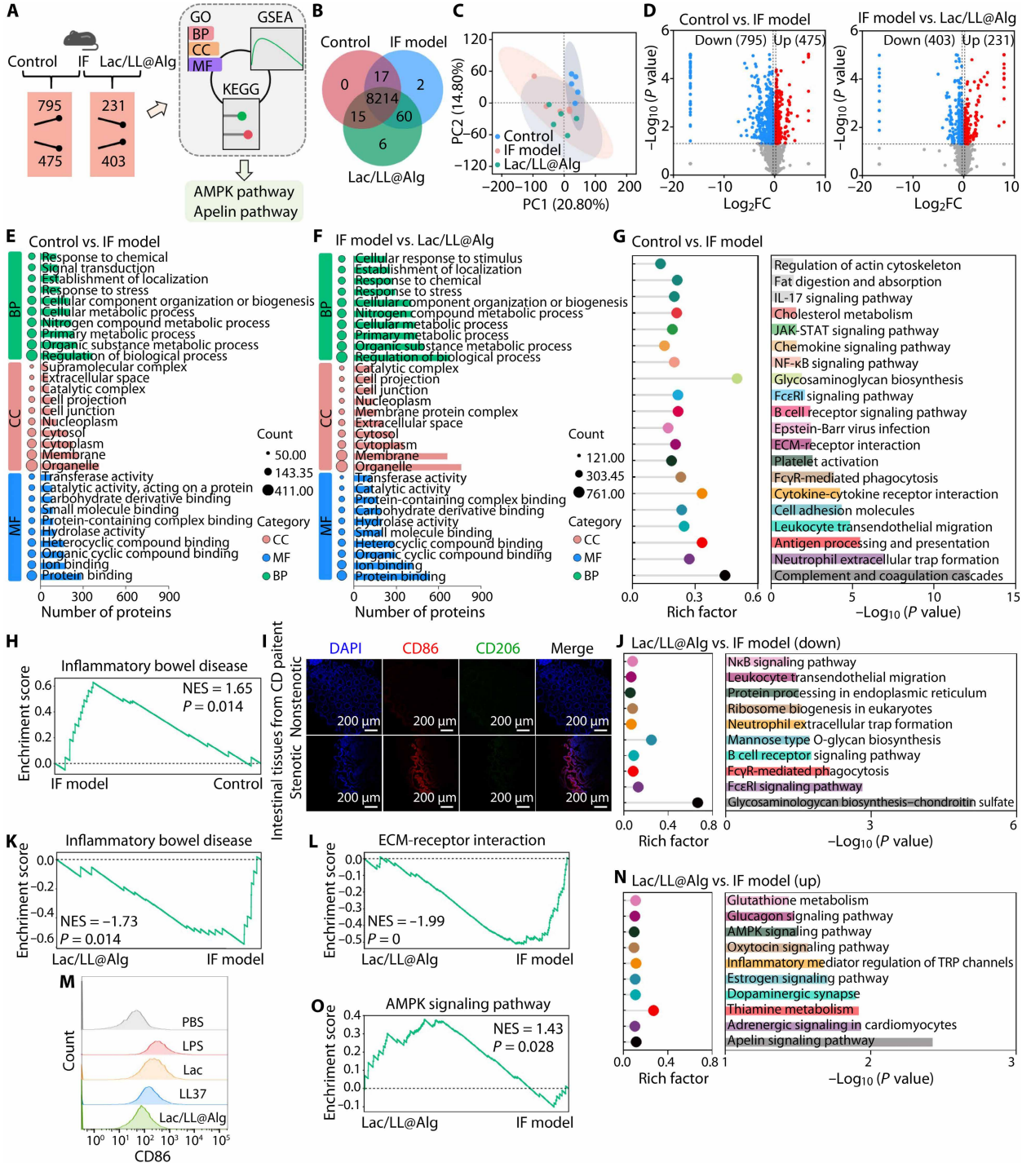


Fig. 9. Protein-level reconfiguration by BTB-Alg treatment. (**A**) The workflow for proteomics analysis. (**B**) The DEPs evaluated using a Venn diagram. (**C**) Principal components analysis of proteomic profiles. (**D**) Volcano plots displaying DEPs in the IF group against the control or Lac/LL@Alg group. The red color indicated that the proteins were up-regulated; the blue color indicated that the proteins were down-regulated. FC, fold change. (**E** and **F**) GO pathway enrichment analysis of DEPs between the IF model and control (E) or Lac/LL@Alg (F) groups. (**G**) KEGG pathway enrichment analysis of DEPs between the IF model and control groups. JAK-STAT, Janus kinase–signal transducer and activator of transcription. (**H**) GSEA of the IBD pathway in colon tissues from control and IF model groups. (**I**) Immunofluorescence staining of macrophages from healthy versus fibrotic intestinal tissues ($n = 3$). CD86 staining (red): M1 macrophage; CD206 staining (green): M2 macrophage. Scale bars, 200 μm. (**J**) KEGG pathway enrichment analysis of DEPs between IF model and Lac/LL@Alg-treated group. (**K** and **L**) GSEA of IBD pathway (K) and ECM-receptor interaction (L) in colon tissues after Lac/LL@Alg treatment. (**M**) Macrophage polarization changes after different treatments ($n = 3$). (**N**) KEGG pathway enrichment analysis of DEPs elucidating therapeutic mechanisms of Lac/LL@Alg in IF. TRP, transient receptor potential. (**O**) GSEA demonstrating AMPK pathway activation by Lac/LL@Alg treatment in colonic tissues. In (B) to (H), (J) to (L), and (N) and (O), data are from $n = 5$ biological replicates. NES, normalized enrichment score.

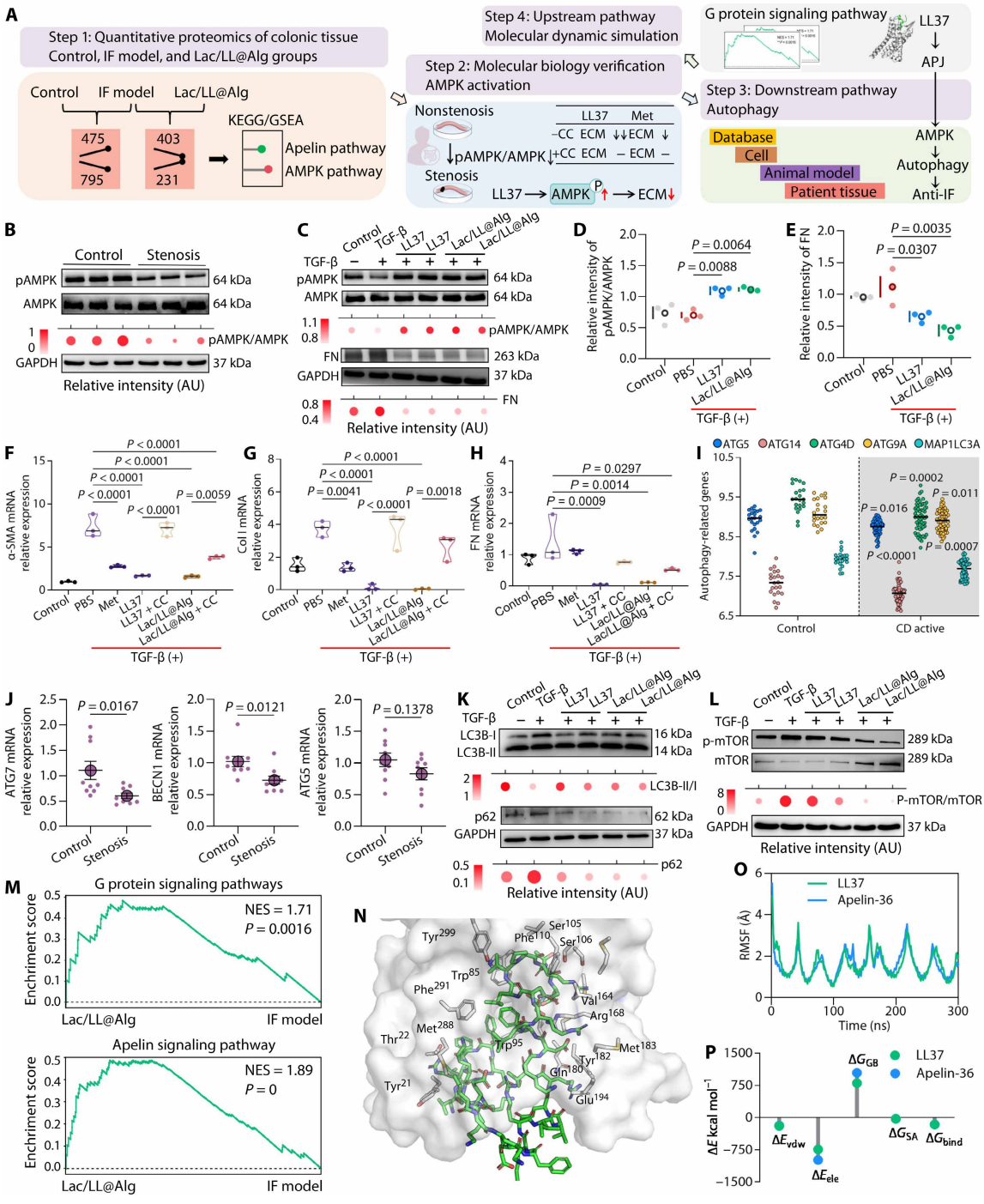


Fig. 10. Molecular investigation of antifibrotic mechanism. (**A**) Workflow for antifibrotic mechanism investigation. (**B**) AMPK activation levels in intestinal stricture tissues versus normal tissues from patients with CD. (**C**) Western blot analysis of AMPK activation and fibrotic marker gene expression after treatment with LL37 or Lac/LL@Alg (C_{LL37} = 20 μg ml^{-1}). (**D** and **E**) Grayscale analysis of Western blot bands for phospho-AMPK (pAMPK)/AMPK (D) and FN (E). (**F** to **H**) qPCR level of α-SMA (F), Col1α1 (G), and FN (H) in CCD-18Co cells after different treatments. (**I**) Expression levels of autophagy-related genes between patients with active-stage CD and healthy controls in the GSE75214 dataset. (**J**) Dysregulation of autophagy-related genes in structured intestinal tissues compared to nonstructured tissues from patients with CD (n = 9). (**K** and **L**) Autophagic flux dynamics were quantified through LC3B-II/I ratio modulation, p62 accumulation (K), and phospho-mTOR signaling activity (L). (**M**) GSEA of G protein signaling pathways and apelin signaling pathway activation in colon tissues after Lac/LL@Alg treatment. (**N**) Dynamic snapshot of the interaction between LL37 and apelin receptor (APJ). (**O**) Root mean square fluctuation (RMSF) analysis of the LL37-APJ and apelin-36–APJ complexes. (**P**) Average binding free energies of the simulated LL37-APJ or apelin-APJ complexes. In (B), (C), (K), (L), and (M) to (P), experiments were repeated three times with consistent results. In (D) to (H), data are shown as mean ± SD (n = 3 biological replicates). Statistical analysis was studied via one-way ANOVA comparing phosphate-buffered saline (PBS), Met, LL37, LL37 + CC, Lac/LL@Alg, and Lac/LL@Alg + CC.

DISCUSSION

In this study, we developed an integrated BTB platform through biomimicry of natural bacterial physiological behaviors, leveraging physical interactions to achieve spatiotemporal synchronization of bioactive components and mechanistic complementarity without formulation-derived toxicity. We explored three key challenges:

What are effective therapeutic strategies for IBD-related complications? IBD-associated fibrosis and CDI constitute the primary cause of disease-related mortality. Here, BTB demonstrates unique advantages by suppressing inflammation while concurrently preventing fibrotic progression and infectious complications. In the context of CDI, the toxins secreted by *C. difficile* directly damage the fragile intestinal barrier in IBD. Furthermore, *C. difficile* further exacerbates intestinal microbial imbalance by reducing beneficial bacteria (*41*). Concurrently, CDI triggers a more intense inflammatory response in IBD, inducing the migration and aggregation of leukocytes. Therefore, in clinical settings, when patients with IBD experience a sudden worsening of symptoms, it is standard practice to rule out CDI. LL37 alleviates *C. difficile*–induced colitis primarily by inhibiting toxin-mediated intestinal inflammation and modulating the immune response. In addition, LL37 exhibits direct antimicrobial activity against *C. difficile* vegetative cells and substantially reduces spore outgrowth, collectively contributing to its therapeutic potential (*42*). With BTB, probiotics and peptides work synergistically to exert anti-inflammatory, immunomodulatory, and microbiota-regulating effects. Notably, LL37 uniquely regulates the activity of myofibroblasts. Consequently, this multimodal integration establishes a platform effect, offering broad-spectrum therapeutic efficacy against IBD and its associated complications.

What are optimal approaches for oral-targeted delivery of LL37 and probiotics? In this study, Lac was chosen as a carrier for LL37 because of its effectiveness in reducing fibrosis, which goes beyond the usual modulation of the microbiota (*43*, *44*) (table S1). Furthermore, Lac in BTB uses nonspecific mechanisms to competitively exclude pathogens, including *C. difficile*. It also demonstrates the ability to protect epithelial cells in vitro through the neutralization of toxins (*45*). While synthetic biology can also engineer microbes to carry peptides, their utility is constrained by limited strain compatibility and biosafety concerns from chromosomal integration (*46*). Our bioinspired engineering approach imposes no restrictions on bacterial types and minimally affects probiotic viability or peptide bioactivity. The Alg layer effectively prevents digestive enzymes from penetrating the BTB surface and also blocks the premature release of LL37 into the external environment, thereby enhancing the stability of biotherapeutics as they transit through the GI tract. Furthermore, the Alg shell interacts with the intestinal mucus layer through hydrogen bonding and polymer chain entanglement, which enhances adhesion and prolongs the retention time of the delivery system within the intestine (Fig. 4) (*47*, *48*). The immunogenicity of Lac was also reduced by the Alg coating layer, leading to successful Lac colonization across all murine models (Figs. 5R and 8F and fig. S13G). Upon reaching the alkaline conditions of the intestine, the Alg layer swells and dissociates, enabling the targeted and programmed release of the cargo (probiotics and LL37) (Fig. 3H). The controlled dissolution of the Alg layer further supports nutrient diffusion for probiotic metabolism and enables a spatiotemporally controlled release of LL37 within specific intestinal niches.

What molecular mechanisms underlie the antifibrotic effects of LL37? Using integrated multiomics, we identified LL37 exerts antifibrotic effects through AMPK-mediated autophagy activation as the core mechanism. We further discussed the potential pathway of autophagy in down-regulating fibrosis. Accumulating evidence suggests that senescence plays key roles in regulating fibrotic processes in multiple organs, including the lung, kidney, and heart (*49*–*52*). One of the most widely recognized features associated with senescence is the senescence-associated secretory phenotype (SASP). The SASP consists of an array of inflammatory mediators, including TGF-β, matrix metalloproteinase 1 (MMP1), and MMP3, which trigger myofibroblast differentiation (*53*). The restoration of autophagic flux has been demonstrated to alleviate senescence and the subsequent fibroblast-to-myofibroblast transdifferentiation (FMT), whereas the inhibition of autophagy can trigger both senescence and FMT (*54*). Previous studies have demonstrated that promoting autophagy in senescent fibroblasts can inhibit cardiac and pulmonary fibrosis (*55*, *56*). Therefore, we speculate that the improvement of IF by AMPK-autophagy observed in this study may be related to its regulation of senescence in activated intestinal fibroblasts. In subsequent research, we will continue to investigate the complex interplay between autophagy and senescence in IF progression and further explore potential drug targets for preventing and treating IBD-related fibrosis.

Drawing inspiration from nature, we established a paradigm for oral biotherapeutics that optimizes stability-efficacy balance in codelivery systems. The clinical translation of probiotic-based delivery platforms also faces several challenges. First, deficiencies in specific probiotic species among patients may vary, necessitating more personalized supplementation strategies. Second, regarding probiotics as drug carriers, variations in surface charge characteristics can occur not only among different bacterial strains but also between various batches of the same strain. Consequently, this may result in inconsistencies in drug loading capacity from batch to batch. Third, maintaining the viability and stability of live bacterial agents during storage and transport is critical, potentially necessitating the use of cold chain logistics or advanced freeze-drying techniques. Despite these challenges, the BTB-Alg also offers insights into next-generation biotherapeutics: (i) design inspiration originating from nature, (ii) pathophysiology-driven material design, and (iii) therapeutic synergism through bioengineering. Briefly, its modular design adapts to other fibrotic disorders (e.g., pulmonary or liver fibrosis), redefining biotherapeutic development for multifactorial diseases.

MATERIALS AND METHODS

Materials

LL37 (sequence: LLGDFFRKSKEKIGKEFKRIVQRIKDFLRNLVP RTES) was purchased from Go Top Peptide Biotech (Hangzhou, China). Alginate (CAS: 9005-38-3; 100 to 200 mPa·s) was acquired from TCI Development Co. Ltd. (Shanghai, China). DSS was acquired from MP Biomedicals (molecular weight: 36,000–50,000 kDa; USA). Mucin was purchased from Psaitong (M10088, China). All ingredients were of pharmaceutical grade. Cell Counting Kit-8 (CCK-8) was obtained from Beyotime Biotechnology (Shanghai, China). TNF-α, IL-17, and IL-1β enzyme-linked immunosorbent assay kits were obtained from Jiangsu Jingmei Biotechnology Co. Ltd. (Jiangsu, China). MPO and MDA detection kits were purchased from Jiangsu Aidisheng Biotechnology Co. Ltd. (Jiangsu, China). All ingredients were of pharmaceutical grade.

Source of strains

Lac was acquired from the BeNa Culture Collection (Beijing, China). A commercial MRS broth acquired from Beijing Land Bridge Technology Limited (Beijing, China) was used as the medium for culturing Lac. Lac was cultured in MRS broth in a shaker (200 rpm at 37°C). *C. difficile* VPI10463 (American Type Culture Collection, 43255) was purchased from the Bio-Science Technology Co. Ltd. (Hangzhou, China).

Ethical statement

All experimental procedures involving animals were conducted in compliance with relevant ethical regulations. Experimental protocols involving animals were conformed to the Chinese Guidelines for the Care and Use of Laboratory Animals. Mice were housed in a specific pathogen–free environment as approved by the Institutional Animal Care and Use Committee (IACUC) of the Zhejiang Center of Laboratory Animals (protocol number: ZJCLA-IACUC-20010840). The collection of patient data and samples was approved by the Ethics Committee of the Zhejiang University (protocol number: [2025B] NO. 0762).

Cells, animals, and patient samples

HT29 cells were bought in the Procell Life Science & Technology Co. Ltd. (Wuhan, China). The Dulbecco's Modified Eagle's Medium High Glucose with L-Glutamine and penicillin-streptomycin (P-S; KeyGEN BioTECH, Jiangning, Nanjing, China), fetal bovine serum (FBS; Biosharp, Beijing, China), and nonessential amino acid (Yuanye Bio-Technology Co. Ltd., Shanghai, China) was used to culture the cells at 37°C in 5% CO_2. CCD-18Co cells were bought in the Cell Bank, Chinese Academy of Sciences. CCD-18Co cells were cultured in Minimum Essential Medium containing nonessential amino acid (number MP150410, Procell, Wuhan, China) supplemented with FBS and P-S (number PB180120, Procell, Wuhan, China).

Sprague-Dawley (SD) rats (6 to 8 weeks) about 200 ± 20 g and C57BL/6 male mice (6 to 8 weeks) about 20 ± 2 g were bought in the Zhejiang Center of Laboratory Animals (Hangzhou, China). SD rats and C57BL/6 mice in this study were maintained with an environment at the constant temperature of 22°C with a dark and light alternation with every other 12 hours. The researchers performing the treatments were blinded to the animal groups.

Intestinal biopsy samples were collected from 10 adult Chinese patients with CD and intestinal stenosis (five males and five females; age range: 19 to 59 years), who informed consented to donate their biological samples at the Department of Gastroenterology, The First Affiliated Hospital, Zhejiang University School of Medicine. During colonoscopy, each patient received three stenosis biopsies or three nonstenosis biopsies.

In vitro assay of antifibrosis effects

CCD-18Co cells (1×10^5) were seeded into six-well plant, allowing for attachment for 24 hours. Then, a mixture solution of TGF-β (10 ng ml^{-1}; PeproTech Inc., New Jersey, USA) with LL37 ($C_{LL37\text{-}1}$ = 1.11 μM or $C_{LL37\text{-}2}$ = 11.1 μM) or Lac/LL@Alg ($C_{LL37\text{-}1}$ = 1.11 μM or $C_{LL37\text{-}2}$ = 11.1 μM) was added. CCD-18Co without TGF-β stimulation was served as a control. The fibrosis-associated factors, such as Col I, α-SMA, and FN, were assayed by the method of reverse transcription quantitative polymerase chain reaction (RT-qPCR). Specifically, we first got the cDNA based on the RT from the extracted RNA via the PrimeScript RT reagent Kit (Takara). The Real-Time PCR System (ABI 7500, Applied Biosystems, CA) was taken advantage of to manipulate the process. Glyceraldehyde-3-phosphate dehydrogenase (GAPDH) was used as a control, which was calculated by a $2^{-\Delta\Delta Ct}$ method. We listed the primer sequences in table S3.

The CCD-18Co cells were seeded into six-well plant, allowing for attachment. Subsequently, the cells were treated with TGF-β (10 ng ml^{-1}) and LL37 ($C_{LL37\text{-}1}$ = 1.11 μM or $C_{LL37\text{-}2}$ = 11.1 μM) for a further 24-hour incubation, respectively. The unstimulated CCD-18Co cells were used as a control. The CCD-18Co cells were collected and healed using radioimmunoprecipitation assay buffer with protease inhibitor cocktail. Proteins (30 μg $sample^{-1}$) were divided by 8% SDS–polyacrylamide gel electrophoresis (SDS-PAGE). After that, polyvinylidene difluoride membranes were used to take the proteins. The membranes were incubated with different primary antibodies for 12 hours after treating with the prepared bovine serum albumin (5%) at 4°C. Then, secondary antibodies were added at 25°C, after washing using Tris-buffered saline with tween 20 (TBST) in a shaker (70 rpm) for three times. After incubation, the proteins on the membranes were identified using ChemiScope 6000 Pro Touch (Clinx Science Instruments Co. Ltd., Shanghai, China). GAPDH was used as internal controls to normalize protein expression. The experiments were triplicated to ensure reliability. Antibodies used for Western blot are listed: Col1α1 [Cell Signaling Technology (CST), #91144], FN (Proteintech, #15613-1-AP), and GAPDH (CST, #5174).

Cell viability assay

HT29 cells (3.0×10^3 per well) were cultured into a 96-well plate. After that, 40 μl of LL37 solutions (2.23, 3.34, 5.575, 11.15, 22.3, and 44.6 μM) were added for further 24 hours of incubation, respectively. The negative control was added with 0.9% NaCl solution. Stimulated CCD-18Co cells (1.6×10^3 per well) with or without TGF-β (10 ng ml^{-1}) were cultured into a 96-well plate, allowing for attachment. After that, 40 μl of LL37 solutions (2.23, 3.34, 5.575, 11.15, 22.3, and 44.6 μM) were added for further 24 hours of incubation, respectively. The fibroblasts derived from patients with CD and Raw 264.7 were treated as the same method as above. Cell viability was assayed with the method of CCK-8 as follows: CCK-8 solution (20 μl) was supplemented in the 96-well plate. Then, we recorded the absorbance (A = 450 nm) of solution by the microplate spectrophotometer (Synergy H1 microplate reader, BioTek). The proliferation viability of the cells was calculated by the following formula

$$\text{Cell viability (\%)} = \frac{A_{\text{treated}}}{A_{\text{control}}} \times 100\,\% \quad (1)$$

Affinity of LL37 to intestinal fibroblasts

CCD-18Co cells (1×10^5) were cultured into a six-well plate, allowing for attachment for 24 hours. Then, FITC-labeled LL37 (LL37-equiv. concentration: 4.45 μM) solution was added, with or without TGF-β. After 2 hours of incubation, cells were collected, and fluorescence intensities were detected using a BD FACSVerse flow cytometer (BD Biosciences, USA).

In another group, CCD-18Co cells were cultured into a six-well plate, allowing for attachment for 24 hours. Then, FITC-labeled LL37 (LL37-equiv. concentration: 4.45 μM) solution was added, with or without TGF-β. Two hours of incubation later, cells were collected and treated with 10% goat serum in phosphate-buffered saline with Tween 20 (PBST) solution. Then, primary antibodies [α-SMA and fibroblast activation protein (FAP)] (Abcam, ab7817; Abcam, ab207178) were added at 4°C. Twelve hours later, we washed three times the paraffin sections with cold PBS solution, which further treated by the secondary antibody under the conditions of

25°C in a dark environment. Last, tissue sections were counterstained with 4′,6-diamidino-2-phenylindole (DAPI) (Beyotime, Shanghai) for 10 min, washed, and observed using a CLSM (Leica, Weztlar, Germany).

Detection on growth curve of Lac

The native Lac was diluted to reach an optical density at 600 nm (OD_{600}) value of 0.2 and spread on a 96-well plate. Then, Lac was supplemented with LL37 solution at 222, 445, or 890 μM, respectively, and kept at 37°C in a shaker (200 rpm). We tested the OD_{600} every 2 hours during the 24 hours with a microplate spectrophotometer. The growth curve of Lac/LL@Alg was determined by the same method. The Alg solutions at concentrations of 0.5, 2, 5, and 10 mg ml^{-1} were uniformly incorporated into Lac cultures in the same method.

Screen and fabrication of BTB-Alg

FITC-labeled LL37 solutions (1 ml; at an LL37-equiv. concentration of 8.34, 16.7, 33.4, 66.8, 134, 223, 334, and 556 μM) were incubated with 1×10^9 CFU of Lac for 30 min, respectively. Then, the Lac/$LL_{1–8}$ was gathered by centrifugation (4000 rpm for 10 min) and detected with the flow cytometer. The supernatants from Lac/$LL_{5–7}$ were collected for high-performance liquid chromatography (HPLC; LC-SPD-M20A, Shimadzu, Japan) detection at 220 nm. The liquid phase conditions were as follows: mobile phase A (0.1% trifluoroacetic acid–H_2O) and phase B (0.1% trifluoroacetic acid–acetonitrile) were set from 65:35 to 35:65. Lac/LL (containing 1×10^9 CFU of Lac and 853 μg of LL37) was suspended in a 1-ml solution of Cy5.5-labeled Alg (at an Alg-equiv. concentration of 0.032, 0.063, 0.125, 0.25, 0.5, 1, or 2 mg ml^{-1}) for 10 min in a shaker. Then, the Lac/LL@$Alg_{1–7}$ was collected by centrifugation (8000 rpm for 10 min). Lac/LL@Alg was resuspended and detected with flow cytometer. For screening the optimal dosage of Alg, the Lac/LL was suspended in 1 ml of 2, 5, or 10 mg ml^{-1} of Alg solution for 10 min in a shaker, respectively. After centrifugation, the sediment was washed three times with PBS, obtaining Lac/LL@Alg-2, Lac/LL@Alg-5, and Lac/LL@Alg-10, which were incubated in 0.5 ml of SGF (pH 1.2) at 37°C for 2 hours. Subsequently, precipitations were separated and further treated with 0.5 ml of 2% SDS overnight. Then, the suspensions were centrifuged (6000 rpm for 5 min) for gathering the supernatant. A 0.2-ml supernatant was treated with 1.8 ml of methanol, and the precipitations were collected by centrifugation (8000 rpm for 5 min). The precipitations collected were resuspended with 0.1 ml of methanol–10 mM sodium carbonate [1:1 (v/v)]. Subsequently, 0.9 ml of methanol was added and thoroughly mixed. The homogenized mixture was then centrifuged (10,000 rpm for 10 min), collected, and subjected to HPLC analysis. Lac/LL@Alg incubated in water was taken as a control.

Characterization of BTB-Alg

The zeta potential and size of Lac, LL37, Alg, Lac/LL, and Lac/LL@Alg were determined using a Zetasizer (Nano ZS90, Malvern, UK). The native Lac and Lac/LL@Alg were washed twice with double distilled H_2O and dripped onto a carbon-coated copper grid for transmission electron microscopy (TEM; HT-7800, Hitachi, Japan). The fluorescently labeled Lac/LL@Alg was fabricated as the above method with FITC-labeled Lac, Cy3-labeled LL37, and Cy5-labeled Alg. The structure of fluorescently labeled Lac/LL@Alg was detected by the CLSM and taken pictures, respectively. An appropriate amount of lyophilized Lac, LL37, Alg, and lyophilized Lac/LL@Alg was determined by XRD (X'Pert^3 Powder, Panalytical, Netherlands), separately. The scanning range (2θ) was set to 5° to 30° with the scanning speed at 2° min^{-1}. The fluorescently labeled Lac/LL@Alg was resuspended into SGF supplemented with pepsin at 37°C. Two hours later, the fluorescently labeled Lac/LL@Alg was collected, washed with PBS, and further resuspended into SIF (pH 7.4) supplemented with trypsin at 37°C for 2, 4, 6, and 8 hours. At set intervals, the fluorescently labeled Lac/LL@Alg was detected by the CLSM and taken pictures. Last, the fluorescently labeled Lac/LL@Alg was collected and resuspended in MRS for further 24 hours. As the same procedure, the same amounts of Lac (1×10^9 CFU) or Lac/LL@Alg (1×10^9 CFU) were resuspended into SGF supplemented with pepsin. Two hours later, the Lac and Lac/LL@Alg were transfer to SIF supplemented with trypsin for further incubation, and samples (50 μl) at different times were collected. After dilution, the collected suspensions were cultured on solid modified MRS medium base plates at 37°C. Twenty-four hours later, we count the colony count. LL37 was substituted with Cy5-labeled LL37 for preparing the Cy5-labeled Lac/LL and Lac/LL@Alg. Then, Cy5-labeled Lac/LL and Lac/LL@Alg were incubated in 0.5 ml of SGF for 2 hours. Subsequently, the suspensions were centrifuged (4000 rpm for 5 min) and transfer to SIF at 37°C for further incubation. Samples were collected at the setting time above and detected by microplate spectrophotometer to calculate the release of LL37.

Establishment of IF mice models

C57BL/6 mice were used to build the colitis-associated IF model by orally administrated with 3 cycles of DSS solutions. Specifically, in the beginning of each cycle, the mice were treated with 2% DSS (w/v) solution for 1 week. Subsequently, the DSS solution was removed, and the mice were treated with water for the following 14 days.

In vivo GI retention and mucoadhesion study

C57BL/6 mice of DSS-induced IF model were orally administered with 200 μl of FITC-labeled Lac, Cy5.5-labeled LL37, or fluorescently labeled Lac/LL@Alg (FITC-labeled Lac, Cy5.5-labeled LL37/, or ICG-labeled Alg), respectively. The oral administration dosage for each group guaranteeing the fluorescence intensity of native Lac and free LL37 was equivalent to Lac and free LL37 in Lac/LL@Alg (tables S5 and S6). Mice were euthanized, and their organs (GI tract, heart, liver, spleen, lungs, and kidneys) were obtained at the setting times (2, 4, 6, and 8 hours). Organs were washed with cold PBS and were imaged and quantified using a VISQUE imaging system (InVivo Smart-LF, Vieworks, Korea). Then, the colonic tissues were cut open, imaged, and quantified with the in vivo imaging system. The fluorescence intensity was recorded for FITC-labeled Lac, Cy5.5-labeled LL37, and ICG-labeled Alg at excitation/emission (Ex/Em) of 490/520, 673/707, and 785/821 nm.

Permeability in mucus barrier

The mucus-penetrating ability of Lac/LL@Alg was monitored by an in vitro GI simulation mucus model. Specifically, 2 ml of fresh mucus collected from the rat intestinal tract was added into a tube. A total of 100 μl of FITC-labeled Lac, Cy5.5-labeled LL37, and Lac/LL@Alg (FITC-labeled Lac and Cy3-labeled LL37) was exposed on the top layer of the diffusion medium at 37°C and allowed to free diffuse (n = 3). Then, the depth of penetration was recorded and photographed. At 0, 8, and 24 hours, 50 μl of sample was separated

from the bottom of the tube, and the fluorescence intensity was recorded at Ex/Em: 490/520 and 673/707 nm). The particle penetration ratio was acquired as

$$\text{Particle penetration ratio (\%)} = \frac{\text{Fluorescence intensity}_{\text{initial}}}{\text{Fluorescence intensity}_{\text{bottom}}} \times 100\% \quad (2)$$

Mucosal adhesion and permeation in intestinal tissue from patients with IBD

Ex vivo human intestinal tissues were secured in a six-well culture plate and equilibrated in oxygenated Tyrode's solution (37°C). Fluorescently labeled Lac/LL@Alg (100 μl) was administered to the luminal surface and incubated for 4 hours. Postincubation, tissues underwent three sequential washes with ice-cold PBS to remove unbound particles. Subsequently, tissues were embedded in optimal cutting temperature compound, rapidly frozen by liquid nitrogen, and cryosectioned into 10-μm slices using a Leica CM1950 cryostat. After that, the sections were stained with DAPI at room temperature for nuclear counterstaining for 10 min. Fluorescence localization was visualized using a CLSM, with Ex/Em settings optimized for FITC (490/520 nm), Cy5.5 (673/707 nm), and DAPI (340/488 nm), respectively.

Therapeutic efficacy on AC

C57BL/6 mice were oral administered 2.5% DSS (w/v) solution daily from the days of 0 to 7 to establish AC mice model, and then mice were separated into five groups for oral administration of different formations every day in the AC model: control group (water); AC model (2.5% DSS + saline); LL37 group (2.5% DSS + 20 mg kg^{-1} of LL37); Lac group (2.5% DSS + 2.3×10^{10} CFU kg^{-1} of Lac); Lac/LL@Alg group (2.5% DSS + 2.3×10^{10} CFU kg^{-1} of Lac and 20 mg kg^{-1} of LL37). The body weights of mice were recorded every day. Feces from these groups were gathered for 16*S* analysis on the last day. After mice were euthanized, and the colons were collected with lengths recorded and photographed. Histologic score and DAI were calculated according to tables S7 and S8. Intestinal weight index and spleen weight index were calculated as follows

$$\text{Intestinal weight index} = \frac{\text{Weight of intestine}}{\text{Length of intestine}} \times 100 \quad (3)$$

$$\text{Spleen weight index} = \frac{\text{Weight of spleen}}{\text{Weight of body}} \times 100 \quad (4)$$

Colonic tissues from different groups were dissected into small fragments and added to a clean Eppendorf tube with 0.9% NaCl solution (1:3). The mixture was homogenized (60 Hz for 120 s) and incubated on ice for 30 min. Afterward, the mixture solution was centrifuged at 3000 rpm for 15 min. Resulting supernatants was used for quantification of IL-10, MDA, and MPO analysis. Peripheral blood samples were collected and centrifuged. Serum TNF-α levels were determined using an enzyme-linked immunosorbent assay kit.

Therapeutic efficacy on DSS and *C. difficile*–induced colitis

C57BL/6 mice were used to establish the DSS and *C. difficile*–induced colitis. Specifically, mice were given 2% DSS (w/v) solution for 5 days and changed to *C. difficile* (1.5×10^9 CFU kg^{-1}) for the following 2 days. Then, feces from these groups were gathered for TcdB detection via RT-qPCR. Total genomic DNA was extracted via the TIANamp Stool DNA Kit (Tiangen Biotech, China). The universal total bacterial 16*S* rRNA was used as an internal control. The sequences of primers were showed in table S3. To evaluate the therapeutic effects, mice were divided into eight groups for oral administration of different formations for 6 days consecutively: control group (water); CD group (1.5×10^9 CFU kg^{-1} of *C. difficile*); DSS group (2% DSS); saline group (2% DSS + 1.5×10^9 CFU kg^{-1} of *C. difficile*); VAN (2% DSS + 1.5×10^9 CFU kg^{-1} of *C. difficile*; 25 mg kg^{-1} of VAN); LL37 group (2% DSS + 1.5×10^9 CFU kg^{-1} of *C. difficile*; 20 mg kg^{-1} of LL37); Lac group (2% DSS + 1.5×10^9 CFU kg^{-1} of *C. difficile*; 2.3×10^{10} CFU kg^{-1} of Lac); Lac/LL@Alg group (2% DSS + 1.5×10^9 CFU kg^{-1} of *C. difficile*; 2.3×10^{10} CFU kg^{-1} of Lac and 20 mg kg^{-1} of LL37). The body weights of mice were recorded every day. Feces from these groups were gathered for 16*S* analysis on the last day. After mice in this study were euthanized, the colons were collected with lengths recorded and photographed. mRNA levels of IL-6, IL-17, and IL-1β were detected by qPCR. The primer sequences were listed in table S3. Colonic tissue specimens were fixed in 4% paraformaldehyde and then infiltrated with paraffin wax. The paraffin underwent conventional dewaxing for hematoxylin and eosin (H&E) staining and immunostaining. For subsequent staining, the sections were immersed in gradient ethanol to get deparaffinized and rehydrated. Endogenous peroxidase activity was quenched by incubating tissue sections in 3% H_2O_2 for 10 min. Next, after antigen retrieval in citrate buffer, the sections were blocked in 5% FBS for an hour at 37°C and then incubated with different primary antibodies (ZO-1, CD86, and CD206) at 4°C overnight. For immunohistochemistry (IHC) staining, 3,3′-diaminobenzidine substrate was used for detection. For immunofluorescence staining, the primary antibodies were incubated with relative secondary antibodies containing different dye, and DAPI was used as nuclear counterstain.

Therapeutic efficacy on murine model of colitis-associated IF

To evaluate the therapeutic effects on chronic colitis-associated IF, mice were divided into five groups for oral administration of different treatments every other day: control group (water); IF model group (2% DSS); LL37 group (2% DSS + 20 mg kg^{-1} of LL37); Lac group (2% DSS + 2.3×10^{10} CFU kg^{-1} of Lac), and Lac/LL@Alg group (2% DSS + 2.3×10^{10} CFU kg^{-1} of Lac and 20 mg kg^{-1} of LL37). During the whole experiment, we tested the body weights of mice in different groups at the days 1, 3, and 5 every week. Feces from control, IF model, and Lac/LL@Alg were gathered for macrogenomic analysis on the last day. After the mice in different groups were euthanized, colon lengths were recorded and photographed. Then, colonic tissues collected (50 mg for each group) were gathered for proteomics analysis.

Histological section

Colonic tissues harvested were added into 4% formalin solution and then embedded in paraffin. The paraffin underwent conventional dewaxing for H&E staining (Servicebio, G1076), Alcian blue-periodic acid schiff (AB-PAS) staining (Servicebio, GP1041), Masson's trichrome staining (Servicebio, G1006), and Van Gieson (VG) staining (Servicebio, G1046). The histological score of colitis was calculated on the basis of the sum of the severity as showed in table S7. Fibrosis score was calculated on the basis of the sum of fibrosis severity as showed in table S9. The expressions of Col I (Servicebio, GB11022-3) and α-SMA (Servicebio, GB12045) were evaluated using IHC. Sections were inspected with a light microscope (Olympus, Tokyo, Japan).

Immunofluorescence staining and analysis

The colonic tissues were stained for immunofluorescence analysis. First, paraffin sections from the groups of control, IF model, LL37, Lac, and Lac/LL@Alg were treated with 10% goat serum in PBST solution. Then, primary antibodies (Col I, α-SMA, E-cadherin, and vimentin) (Servicebio, GB11022-3, GB12045, GB12083, and GB111308) were added at 4°C. Twelve hours later, we washed the paraffin sections three times with cold PBS solution, which further treated by the secondary antibody under the conditions of 25°C in a dark environment. Last, sections were treated with DAPI and observed with CLSM.

Metagenomic analysis

Fecal samples from the control, IF model, and Lac/LL@Alg were collected for whole-metagenome shotgun sequencing. The genomic DNA was extracted from feces collected from different groups with DNA isolation kit (magnetic bead) (MJYH, Shanghai, China). Then, Synergy HTX and NanoDrop 2000 were applied to detect the quality and concentration of DNA, which was further inspected using 1% agarose gel. After that, the genomic DNA extracted was clipped with an average of ~350 base pairs. The paired-end library was established, and the sequence of these was detected on Illumina NovaSeq X Plus (San Diego, USA). We analyzed the data through the online platform of Majorbio Cloud (www.majorbio.com). Specifically, taking the advantage of CD-HIT instrument (https://github.com/weizhongli/cdhit/releases, version 4.6.1), we established a nonredundant gene catalog. In addition, to get the best-hit taxonomy, we analysis the aligning nonredundant genes according to nonredundant database of the National Center for Biotechnology Information (http://ab.inf.uni-tuebingen.de/software/diamond/, version 2.0.13) at the setting *e* value break for 1×10^{-5}. VFDB was analyzed according to the VFDB (www.mgc.ac.cn/VFs/main.htm). Furthermore, the KEGG pathway database (www.genome.jp/kegg/) was taken advantage for the analysis on functional enrichment annotations in different groups.

Proteomics analysis

The colonic tissues from control, IF model, and Lac/LL@Alg were collected for a four-dimensional data-independent acquisition (DIA)–based proteomics. Proteins were first extracted, digested, desalted, and quantified. Subsequently, peptides collected were analyzed using mass spectrometer 7 (Thermo Fisher Scientific, USA), with μPAC High Throughput column (75 μm × 5.5 cm). The liquid phase conditions were as follows: mobile phase A including water with 2% acetonitrile and 0.1% formic acid and mobile phase B including water with 80% acetonitrile and 0.1% formic acid. DIA data were got by a mass spectrometer (Orbitrap Astral, Thermo Fisher Scientific, France) at 70 to 1050 mass/charge ratio (*m/z*) range for MS1, and 150 to 2000 *m/z* range for MS2. DIA raw data were searched by Spectronaut software (version 18). Protein was identified when had at least one unique peptide. We analyzed the data through the online platform of Majorbio Cloud. DEPs were identified by satisfying the fold change between groups as >1.2 or <0.83 and $P < 0.05$, simultaneously. With the same method as the section of "Metagenomic analysis," functional enrichment annotations were analyzed via KEGG pathway database with Python and GO pathway database with a software goatools (version 1.4.4). The interaction analysis of protein-protein was carried out using the String v11.5. To determine overrepresented or downrepresented gene sets between two to-be-compared groups, we used GSEA (version 4.3.2) as a computational tool.

Macrophage polarization detection

RAW 264.7 murine macrophages were collected and stained with Live/Dead dye (BV510, BD Pharmingen) at 4°C for 15 min. Subsequently, washed twice with staining buffer (PBS with 2% FBS) for 5 min, mouse Fc block (BD Pharmingen) was used at 4°C for 10 min to avoid nonspecific binding. Then, cell surface marker antibodies (BD Pharmingen) were incubated with cells in the dark on ice for 30 min. To be specific, CD11b (BV421, BD Pharmingen) was intended to assure macrophages, CD86 (allophycocyanin, BD Pharmingen)–labeling M1 macrophage, and CD206 (phycoerythrin, BD Pharmingen)–marking M2 macrophage. After another two round of washing, labeled cells were resuspended and detected on BD FACSymphony A5 SE. Data were analyzed by the FlowJo software.

The molecular mechanism of antifibrosis for LL37

The CCD-18Co cells were seeded into six-well plant, allowing for attachment. Subsequently, the cells were treated with TGF-β (10 ng ml^{-1}) and LL37 ($C_{LL37} = 2.22$ μM), or Lac/LL@Alg ($C_{LL37} = 2.22$ μM), for a further 24-hour incubation, respectively. The CCD-18Co cells were collected and healed using radioimmunoprecipitation assay buffer with protease inhibitor cocktail. Proteins (30 μg $sample^{-1}$) were divided by 8% SDS-PAGE. The unstimulated CCD-18Co cells were used as a control. After that, polyvinylidene difluoride membranes were used to take the proteins. The membranes were incubated overnight with different primary antibodies after treating with the prepared bovine serum albumin (5%) at 4°C. Then, secondary antibodies were added at 25°C, after washing three times using TBST in a shaker (70 rpm). After incubation, the proteins on the membranes were identified using ChemiScope 6000 Pro Touch (Clinx Science Instruments Co. Ltd., Shanghai, China). GAPDH was used as internal controls to normalize protein expression. The experiments were triplicated to ensure reliability. Antibodies used for Western blot are listed: phospho-AMPKα (pAMPKα) (CST, #2535), AMPK (ABclonal, #A12718), LC3B (MilliporeSigma, #L7543), p62 (Proteintech, #66184-1-Ig), p-mTOR (CST, #2971), and mTOR (Abcam, #ab134903). Intestinal tissue samples from both stenotic and nonstenotic regions of patients with CD were processed with the same method.

In another group, CCD-18Co cells were plated at a density of 1×10^5 cells per well into six-well plant, allowing for attachment. Then, CCD-18Co cells were stimulated with TGF-β (10 ng ml^{-1}) and treated with PBS, Met (MedChemExpress, HY-B0627) (1.00 mM), LL37 (1.11 μM), LL37 (1.11 μM) + CC (MCE, HY-13418A) (20 μM), Lac/LL@ALg ($C_{LL37} = 1.11$ μM), and Lac/LL@ALg ($C_{LL37} = 1.11$ μM) + CC for 24 hours, respectively. The mRNA levels of Col I, FN, and α-SMA were detected by qPCR with the same method.

Statistical analysis

Statistical analyses were performed using GraphPad Prism 9.0 (GraphPad Software). Data are presented as mean ± SD. When there were more than two groups, intergroup differences were analyzed via one-way analysis of variance (ANOVA) for comparisons. When there were only two groups, intergroup differences were analyzed via student's *t* test unless specifically described. It was considered statistically significant between groups at the condition of $P < 0.05$. Three replicates at lease were performed for the quantitative analysis. The other qualitative or characteristic experiments were independently repeated three times.

Supplementary Materials

This PDF file includes:

Supplementary Text
Figs. S1 to S30
Tables S1 to S9
References

REFERENCES

1. S. D'Alessio, F. Ungaro, D. Noviello, S. Lovisa, L. Peyrin-Biroulet, S. Danese, Revisiting fibrosis in inflammatory bowel disease: The gut thickens. *Nat. Rev. Gastroenterol. Hepatol.* **19**, 169–184 (2022).
2. N. C. Henderson, F. Rieder, T. A. Wynn, Fibrosis: From mechanisms to medicines. *Nature* **587**, 555–566 (2020).
3. N. G. Kotla, S. Rana, G. Sivaraman, O. Sunnapu, P. K. Vemula, A. Pandit, Y. Rochev, Bioresponsive drug delivery systems in intestinal inflammation: State-of-the-art and future perspectives. *Adv. Drug Deliv. Rev.* **146**, 248–266 (2019).
4. G. D'Haens, F. Rieder, B. G. Feagan, P. D. R. Higgins, J. Panés, C. Maaser, G. Rogler, M. Löwenberg, R. van der Voort, M. Pinzani, L. Peyrin-Biroulet, S. Danese, International organization for inflammatory bowel disease fibrosis working group, challenges in the pathophysiology, diagnosis, and management of intestinal fibrosis in inflammatory bowel disease. *Gastroenterology* **162**, 26–31 (2022).
5. X. Zhao, W. Yang, T. Yu, Y. Yu, X. Cui, Z. Zhou, H. Yang, Y. Yu, A. J. Bilotta, S. Yao, J. Xu, J. Zhou, G. S. Yochum, W. A. Koltun, A. Portolese, D. Zeng, J. Xie, I. V. Pinchuk, H. Zhang, Y. Cong, Th17 cell-derived amphiregulin promotes colitis-associated intestinal fibrosis through activation of mTOR and MEK in intestinal myofibroblasts. *Gastroenterology* **164**, 89–102 (2023).
6. Z. Yang, J. Qin, L. Zhao, T. Chen, Q. Huang, Y. Jian, Q. Zhao, S. Yang, Q. Li, Q. Liu, M. Otto, M. Li, Host sorbitol and bacterial sorbitol utilization promote *Clostridioides difficile* infection in inflammatory bowel disease. *Gastroenterology* **164**, 1189–1201.e13 (2023).
7. L. K. Kociolek, D. N. Gerding, Breakthroughs in the treatment and prevention of *Clostridium difficile* infection. *Nat. Rev. Gastroenterol. Hepatol.* **13**, 150–160 (2016).
8. X. Liu, S. Chen, J. Huang, Y. Du, Z. Luo, Y. Zhang, L. Liu, Y. Chen, Synthetic polypeptides inhibit nucleic acid-induced inflammation in autoimmune diseases by disrupting multivalent TLR9 binding to LL37-DNA bundles. *Nat. Nanotechnol.* **19**, 1745–1756 (2024).
9. R. Jing, L. Zhang, R. Li, Z. Yang, J. Song, Q. Wang, N. Cao, G. Han, H. Yin, Milk-derived extracellular vesicles functionalized with anti-tumour necrosis factor-α nanobody and anti-microbial peptide alleviate ulcerative colitis in mice. *J. Extracell. Vesicles* **13**, e12462 (2024).
10. J. Ho, H. Chan, Y. Liang, X. Liu, L. Zhang, Q. Li, Y. Zhang, J. Zeng, F. N. Ugwu, I. H. T. Ho, W. Hu, J. C. W. Yau, S. H. Wong, W. T. Wong, L. Ling, C. H. Cho, R. L. Gallo, T. Gin, G. Tse, J. Yu, M. T. V. Chan, C. C. H. Leung, W. K. K. Wu, Cathelicidin preserves intestinal barrier function in polymicrobial sepsis. *Crit. Care* **24**, 47 (2020).
11. T. C. Hing, S. Ho, D. Q. Shih, R. Ichikawa, M. Cheng, J. Chen, X. Chen, I. Law, R. Najarian, C. P. Kelly, R. L. Gallo, S. R. Targan, C. Pothoulakis, H. W. Koon, The antimicrobial peptide cathelicidin modulates *Clostridium difficile*-associated colitis and toxin A-mediated enteritis in mice. *Gut* **62**, 1295–1305 (2013).
12. J. H. Yoo, S. Ho, D. H. Tran, M. Cheng, K. Bakirtzi, Y. Kukota, R. Ichikawa, B. Su, D. H. Tran, T. C. Hing, I. Chang, D. Q. Shih, R. E. Issacson, R. L. Gallo, C. Fiocchi, C. Pothoulakis, H. W. Koon, Antifibrogenic effects of the antimicrobial peptide cathelicidin in murine colitis-associated fibrosis. *Cell. Mol. Gastroenterol. Hepatol.* **1**, 55–74.e1 (2015).
13. I. Sugrue, R. P. Ross, C. Hill, Bacteriocin diversity, function, discovery and application as antimicrobials. *Nat. Rev. Microbiol.* **22**, 556–571 (2024).
14. T. Backman, S. M. Latorre, E. Symeonidi, A. Muszyński, E. Bleak, L. Eads, P. I. Martinez-Koury, S. Som, A. Hawks, A. D. Gloss, D. M. Belnap, A. M. Manuel, A. M. Deutschbauer, J. Bergelson, P. Azadi, H. A. Burbano, T. L. Karasov, A phage tail-like bacteriocin suppresses competitors in metapopulations of pathogenic bacteria. *Science* **384**, eado0713 (2024).
15. J. Kreitz, M. J. Friedrich, A. Guru, B. Lash, M. Saito, R. K. Macrae, F. Zhang, Programmable protein delivery with a bacterial contractile injection system. *Nature* **616**, 357–364 (2023).
16. V. C. Goodoory, M. Khasawneh, C. J. Black, E. M. M. Quigley, P. Moayyedi, A. C. Ford, Efficacy of probiotics in irritable bowel syndrome: Systematic review and meta-analysis. *Gastroenterology* **165**, 1206–1218 (2023).
17. F. Cao, L. Jin, Y. Gao, Y. Ding, H. Wen, Z. Qian, C. Zhang, L. Hong, H. Yang, J. Zhang, Z. Tong, W. Wang, X. Chen, Z. Mao, Artificial-enzymes-armed *Bifidobacterium longum* probiotics for alleviating intestinal inflammation and microbiota dysbiosis. *Nat. Nanotechnol.* **18**, 617–627 (2023).
18. P. Guo, W. Wang, Q. Xiang, C. Pan, Y. Qiu, T. Li, D. Wang, J. Ouyang, R. Jia, M. Shi, Y. Wang, J. Li, J. Zou, Y. Zhong, J. Zhao, D. Zheng, Y. Cui, G. Ma, W. Wei, Engineered probiotic ameliorates ulcerative colitis by restoring gut microbiota and redox homeostasis. *Cell Host Microbe* **32**, 1502–1518.e9 (2024).
19. C. K. I. Jordan, R. L. Brown, M. L. Y. Larkinson, R. P. Sequeira, A. M. Edwards, T. B. Clarke, Symbiotic Firmicutes establish mutualism with the host via innate tolerance and resistance to control systemic immunity. *Cell Host Microbe* **31**, 1433–1449.e9 (2023).
20. L. Jia, Y. Jiang, L. Wu, J. Fu, J. Du, Z. Luo, L. Guo, J. Xu, Y. Liu, *Porphyromonas gingivalis* aggravates colitis via a gut microbiota-linoleic acid metabolism-Th17/Treg cell balance axis. *Nat. Commun.* **15**, 1617 (2024).
21. G. R. Guern, T. Grandjean, S. Stabler, M. Bauduin, P. Gosset, É. Kipnis, R. Dessein, Gut colonisation with multidrug-resistant *Klebsiella pneumoniae* worsens *Pseudomonas aeruginosa* lung infection. *Nat. Commun.* **14**, 78 (2023).
22. P. Feuerstadt, T. J. Louie, B. Lashner, E. E. L. Wang, L. Diao, J. A. Bryant, M. Sims, C. S. Kraft, S. H. Cohen, C. S. Berenson, L. Y. Korman, C. B. Ford, K. D. Litcofsky, M. J. Lombardo, J. R. Wortman, H. Wu, J. G. Auniņš, C. W. J. McChalicher, J. A. Winkler, B. H. McGovern, M. Trucksis, M. R. Henn, L. von Moltke, SER-109, an oral microbiome therapy for recurrent *Clostridioides difficile* infection. *N. Engl. J. Med.* **386**, 220–229 (2022).
23. K. K. Youssef, M. A. Nieto, Epithelial-mesenchymal transition in tissue repair and degeneration. *Nat. Rev. Mol. Cell Biol.* **25**, 720–739 (2024).
24. W. Zhou, W. H. Wu, Z. L. Si, H. L. Liu, H. Wang, H. Jiang, Y. F. Liu, R. N. Alolga, C. Chen, S. J. Liu, X. Y. Bian, J. J. Shan, J. Li, N. H. Tan, Z. H. Zhang, The gut microbe *Bacteroides fragilis* ameliorates renal fibrosis in mice. *Nat. Commun.* **13**, 6081 (2022).
25. H. Kawai, Y. Osawa, M. Matsuda, T. Tsunoda, K. Yanagida, D. Hishikawa, M. Okawara, Y. Sakamoto, T. Shimagaki, Y. Tsutsui, Y. Yoshida, S. Yoshikawa, K. Hashi, H. Doi, T. Mori, T. Yamazoe, S. Yoshio, M. Sugiyama, D. Okuzaki, H. Komatsu, A. Inui, M. Tamura-Nakano, C. Oyama, H. Shindou, H. Kusano, M. Kage, T. Ikegami, K. Yanaga, T. Kanto, Sphingosine-1-phosphate promotes tumor development and liver fibrosis in mouse model of congestive hepatopathy. *Hepatology* **76**, 112–125 (2022).
26. A. Pezone, F. Olivieri, M. V. Napoli, A. Procopio, E. V. Avvedimento, A. Gabrielli, Inflammation and DNA damage: Cause, effect or both. *Nat. Rev. Rheumatol.* **19**, 200–211 (2023).
27. Y. Zhao, M. Simon, A. Seluanov, V. Gorbunova, DNA damage and repair in age-related inflammation. *Nat. Rev. Immunol.* **23**, 75–89 (2022).
28. G. R. Steinberg, D. G. Hardie, New insights into activation and function of the AMPK. *Nat. Rev. Mol. Cell Biol.* **24**, 255–272 (2023).
29. S. Qin, W. Xiao, C. Zhou, Q. Pu, X. Deng, L. Lan, H. Liang, X. Song, M. Wu, Pseudomonas aeruginosa: Pathogenesis, virulence factors, antibiotic resistance, interaction with host, technology advances and emerging therapeutics. *Signal Transduct. Target. Ther.* **7**, 199 (2022).
30. A. Lavelle, H. Sokol, Gut microbiota-derived metabolites as key actors in inflammatory bowel disease. *Nat. Rev. Gastroenterol. Hepatol.* **17**, 223–237 (2020).
31. F. Rieder, P. K. Mukherjee, W. J. Massey, Y. Wang, C. Fiocchi, Fibrosis in IBD: From pathogenesis to therapeutic targets. *Gut* **73**, 854–866 (2024).
32. M. F. Neurath, Strategies for targeting cytokines in inflammatory bowel disease. *Nat. Rev. Immunol.* **24**, 559–576 (2024).
33. D. M. Arenson, D. M. Bissell, Glycosaminoglycan, proteoglycan, and hepatic fibrosis. *Gastroenterology* **92**, 536–538 (1987).
34. E. Hoffman, Y. Song, F. Zhang, L. Asarian, I. Downs, B. Young, X. Han, Y. Ouyang, K. Xia, R. J. Linhardt, D. J. Weiss, Regional and disease-specific glycosaminoglycan composition and function in decellularized human lung extracellular matrix. *Acta Biomater.* **168**, 388–399 (2023).
35. F. Peng, M. Liao, W. Jin, W. Liu, Z. Li, Z. Fan, L. Zou, S. Chen, L. Zhu, Q. Zhao, G. Zhan, L. Ouyang, C. Peng, B. Han, J. Zhang, L. Fu, 2-APQC, a small-molecule activator of sirtuin-3 (SIRT3), alleviates myocardial hypertrophy and fibrosis by regulating mitochondrial homeostasis. *Signal Transduct. Target. Ther.* **9**, 133 (2024).
36. B. Qiu, A. Lawan, C. E. Xirouchaki, J. S. Yi, M. Robert, L. Zhang, W. Brown, C. Fernández-Hernando, X. Yang, T. Tiganis, A. M. Bennett, MKP1 promotes nonalcoholic steatohepatitis by suppressing AMPK activity through LKB1 nuclear retention. *Nat. Commun.* **14**, 5405 (2023).
37. Z. Zou, W. Hu, F. Kang, Z. Xu, Y. Li, J. Zhang, J. Li, Y. Zhang, S. Dong, Interplay between lipid dysregulation and ferroptosis in chondrocytes and the targeted therapy effect of metformin on osteoarthritis. *J. Adv. Res.* **69**, 515–529 (2025).
38. L. Vucicevic, M. Misirkic, K. Janjetovic, U. Vilimanovich, E. Sudar, E. Isenovic, M. Prica, L. Harhaji-Trajkovic, T. Kravic-Stevovic, V. Bumbasirevic, V. Trajkovic, Compound C induces protective autophagy in cancer cells through AMPK inhibition-independent blockade of Akt/mTOR pathway. *Autophagy* **7**, 40–50 (2011).
39. Y. Kwon, S. Mehta, M. Clark, G. Walters, Y. Zhong, H. N. Lee, R. K. Sunahara, J. Zhang, Non-canonical β-adrenergic activation of ERK at endosomes. *Nature* **611**, 173–179 (2022).
40. I. Rodríguez-Espigares, M. Torrens-Fontanals, J. K. S. Tiemann, D. Aranda-García, J. M. Ramírez-Anguita, T. M. Stepniewski, N. Worp, A. Varela-Rial, A. Morales-Pastor, B. Medel-Lacruz, G. Pándy-Szekeres, E. Mayol, T. Giorgino, J. Carlsson, X. Deupi, S. Filipek, M. Filizola, J. C. Gómez-Tamayo, A. Gonzalez, H. Gutiérrez-de-Terán, M. Jiménez-Rosés, W. Jespers, J. Kapla, G. Khelashvili, P. Kolb, D. Latek, M. Marti-Solano, P. Matricon, M. T. Matsoukas, P. Miszta, M. Olivella, L. Perez-Benito, D. Provasi, S. Ríos, I. R. Torrecillas, J. Sallander, A. Sztyler, S. Vasile, H. Weinstein, U. Zachariae, P. W. Hildebrand, G. De Fabritiis,

F. Sanz, D. E. Gloriam, A. Cordomi, R. Guixà-González, J. Selent, GPCRmd uncovers the dynamics of the 3D-GPCRome. *Nat. Methods* **17**, 777–787 (2020).
41. D. Dong, T. Su, W. Chen, D. Wang, Y. Xue, Q. Lu, C. Jiang, Q. Ni, E. Mao, Y. Peng, *Clostridioides difficile* aggravates dextran sulfate solution (DSS)-induced colitis by shaping the gut microbiota and promoting neutrophil recruitment. *Gut Microbes* **15**, 2192478 (2023).
42. R. Liu, J. M. Suárez, B. Weisblum, S. H. Gellman, S. M. McBride, Synthetic polymers active against *Clostridium difficile* vegetative cell growth and spore outgrowth. *J. Am. Chem. Soc.* **136**, 14498–14504 (2014).
43. Y. Hou, L. Zhu, X. Ye, Q. Ke, Q. Zhang, X. Xie, J. G. Piao, Y. Wei, Integrated oral microgel system ameliorates renal fibrosis by hitchhiking co-delivery and targeted gut flora modulation. *J. Nanobiotechnology* **22**, 305 (2024).
44. Y. Liu, K. Chen, F. Li, Z. Gu, Q. Liu, L. He, T. Shao, Q. Song, F. Zhu, L. Zhang, M. Jiang, Y. Zhou, S. Barve, X. Zhang, C. J. McClain, W. Feng, Probiotic *Lactobacillus rhamnosus* GG prevents liver fibrosis through inhibiting hepatic bile acid synthesis and enhancing bile acid excretion in mice. *Hepatology* **71**, 2050–2066 (2020).
45. J. Auclair, M. Frappier, M. Millette, *Lactobacillus acidophilus* CL1285, *Lactobacillus casei* LBC80R, and *Lactobacillus rhamnosus* CLR2 (Bio-K+): Characterization, manufacture, mechanisms of action, and quality control of a specific probiotic combination for primary prevention of *Clostridium difficile* infection. *Clin. Infect. Dis.* **60**, S135–S143 (2015).
46. D. E. Cameron, C. J. Bashor, J. J. Collins, A brief history of synthetic biology. *Nat. Rev. Microbiol.* **12**, 381–390 (2014).
47. L. Zhu, T. Yu, W. Wang, T. Xu, W. Geng, N. Li, X. Zan, Responsively degradable nanoarmor-assisted super resistance and stable colonization of probiotics for enhanced inflammation-targeted delivery. *Adv. Mater.* **36**, e2308728 (2024).
48. G. W. Liu, M. J. Pickett, J. L. P. Kuosmanen, K. Ishida, W. A. M. Madani, G. N. White, J. Jenkins, S. Park, V. R. Feig, M. Jimenez, C. Karavasili, N. B. Lal, M. Murphy, A. Lopes, J. Morimoto, N. Fitzgerald, J. H. Cheah, C. K. Soule, N. Fabian, A. Hayward, R. Langer, G. Traverso, Drinkable in situ-forming tough hydrogels for gastrointestinal therapeutics. *Nat. Mater.* **23**, 1292–1299 (2024).
49. A. R. Baek, J. Hong, K. S. Song, A. S. Jang, D. J. Kim, S. S. Chin, S. W. Park, Spermidine attenuates bleomycin-induced lung fibrosis by inducing autophagy and inhibiting endoplasmic reticulum stress (ERS)-induced cell death in mice. *Exp. Mol. Med.* **52**, 2034–2045 (2020).
50. L. Wang, R. Chen, G. Li, Z. Wang, J. Liu, Y. Liang, J. P. Liu, FBW7 mediates senescence and pulmonary fibrosis through telomere uncapping. *Cell Metab.* **32**, 860–877.e9 (2020).
51. C. Luo, S. Zhou, Z. Zhou, Y. Liu, L. Yang, J. Liu, Y. Zhang, H. Li, Y. Liu, F. F. Hou, L. Zhou, Wnt9a promotes renal fibrosis by accelerating cellular senescence in tubular epithelial cells. *J. Am. Soc. Nephrol.* **29**, 1238–1256 (2018).
52. D. Muñoz-Espín, M. Serrano, Cellular senescence: From physiology to pathology. *Nat. Rev. Mol. Cell Biol.* **15**, 482–496 (2014).
53. S. O'Reilly, P. S. Tsou, J. Varga, Senescence and tissue fibrosis: Opportunities for therapeutic targeting. *Trends Mol. Med.* **30**, 1113–1125 (2024).
54. R. Guan, L. Yuan, J. Li, J. Wang, Z. Li, Z. Cai, H. Guo, Y. Fang, R. Lin, W. Liu, L. Wang, Q. Zheng, J. Xu, Y. Zhou, J. Qian, M. Ding, J. Luo, Y. Li, K. Yang, D. Sun, H. Yao, J. He, W. Lu, Bone morphogenetic protein 4 inhibits pulmonary fibrosis by modulating cellular senescence and mitophagy in lung fibroblasts. *Eur. Respir. J.* **60**, 2102307 (2022).
55. M. Jin, C. Li, Z. Wu, Z. Tang, J. Xie, G. Wei, Z. Yang, S. Huang, Y. Chen, X. Li, Y. Chen, W. Liao, Y. Liao, G. Chen, H. Zheng, J. Bin, Inhibiting the histone demethylase Kdm4a restrains cardiac fibrosis after myocardial infarction by promoting autophagy in premature senescent fibroblasts. *Adv. Sci. (Weinh)* **12**, e2414830 (2025).
56. X. Zhang, X. X. Hu, Y. Q. Zhang, B. Liu, H. H. Pan, Z. K. Liu, Z. M. Yao, Q. X. Zhu, C. H. Wu, T. Shen, Impaired autophagy-accelerated senescence of alveolar type II epithelial cells drives pulmonary fibrosis induced by single-walled carbon nanotubes. *J. Nanobiotechnology* **21**, 69 (2023).
57. S. Lin, G. Xie, J. He, L. Meng, Y. Pang, J. Liu, Enhancing phage therapy by coating single bacteriophage-infected bacteria with polymer to preserve phage vitality. *Nat. Biomed. Eng.* **9**, 1155–1171 (2025).
58. Y. Chen, S. Lin, L. Wang, Y. Zhang, H. Chen, Z. Fu, M. Zhang, H. Luo, J. Liu, Reinforcement of the intestinal mucosal barrier via mucus-penetrating PEGylated bacteria. *Nat. Biomed. Eng.* **8**, 823–841 (2024).
59. Y. Chen, M. Shui, H. Li, M. Guo, Q. Yuan, W. Hao, T. Wang, H. Zhou, Z. Chen, S. Wang, Inflammation-targeted delivery of probiotics for alleviation of colitis and associated cognitive disorders through improved vitality and colonization. *Biomaterials* **318**, 123163 (2025).
60. M. Xu, W. Xin, J. Xu, A. Wang, S. Ma, D. Dai, Y. Wang, D. Yang, L. Zhao, H. Li, Biosilification-mimicking chiral nanostructures for targeted treatment of inflammatory bowel disease. *Nat. Commun.* **16**, 2551 (2025).
61. W. W. Wang, S. Y. Ji, W. Zhang, J. Zhang, C. Cai, R. Hu, S. K. Zang, L. Miao, H. Xu, L. N. Chen, Z. Yang, J. Guo, J. Qin, D. D. Shen, P. Liang, Y. Zhang, Y. Zhang, Structure-based design of non-hypertrophic apelin receptor modulator. *Cell* **187**, 1460–1475.e20 (2024).
62. R. X. Wang, X. L. Fang, Y. Lu, S. M. Wang, The PDBbind database: Collection of binding affinities for protein−ligand complexes with known three-dimensional structures. *J. Med. Chem.* **47**, 2977–2980 (2004).
63. G. M. Sastry, M. Adzhigirey, T. Day, R. Annabhimoju, W. Sherman, Protein and ligand preparation: Parameters, protocols, and influence on virtual screening enrichments. *J. Comput. Aided Mol. Des.* **27**, 221–234 (2013).
64. Y. Zhang, M. F. Sanner, AutoDock crankPep: Combining folding and docking to predict protein-peptide complexes. *Bioinformatics* **35**, 5121–5127 (2019).
65. Y. Zhang, S. Forli, A. Omelchenko, M. F. Sanner, AutoGridFR: Improvements on AutoDock affinity maps and associated software tools. *J. Comput. Chem.* **40**, 2882–2886 (2019).
66. S. Feng, S. Park, Y. K. Choi, W. Im, CHARMM-GUI membrane builder: Past, current, and future developments and applications. *J. Chem. Theory Comput.* **19**, 2161–2185 (2023).
67. W. L. Jorgensen, J. Chandrasekhar, J. D. Madura, R. W. Impey, M. L. Klein, Comparison of simple potential functions for simulating liquid water. *J. Chem. Phys.* **79**, 926–935 (1983).
68. C. Tian, K. Kasavajhala, K. A. A. Belfon, L. Raguette, H. Huang, A. N. Migues, J. Bickel, Y. Wang, J. Pincay, Q. Wu, C. Simmerling, ff19SB: Amino-acid-specific protein backbone parameters trained against quantum mechanics energy surfaces in solution. *J. Chem. Theory Comput.* **16**, 528–552 (2020).
69. C. J. Dickson, B. D. Madej, A. A. Skjevik, R. M. Betz, K. Teigen, I. R. Gould, R. C. Walker, Lipid14: The amber lipid force field. *J. Chem. Theory Comput.* **10**, 865–879 (2014).
70. C. Sagui, T. Darden, Efficient particle-mesh Ewald based approach to fixed and induced dipolar interactions. *J. Chem. Phys.* **113**, 10913–10927 (2000).
71. J. P. Ryckaert, G. Ciccotti, H. J. C. Berendsen, Numerical integration of the cartesian equations of motion of a system with constraints: Molecular dynamics of *n*-alkanes. *J. Chem. Phys.* **23**, 327–341 (1977).
72. A. Onufriev, D. Bashford, D. A. Case, Exploring protein native states and large-scale conformational changes with a modified generalized born model. *Proteins* **55**, 383–394 (2004).
73. G. Weng, E. Wang, F. Chen, H. Sun, Z. Wang, T. Hou, Assessing the performance of MM/PBSA and MM/GBSA methods. 9. Prediction reliability of binding affinities and binding poses for protein-peptide complexes. *Phys. Chem. Chem. Phys.* **21**, 10135–10145 (2019).

Acknowledgments: We thank J. Zhang and X. Chen for animal experiments. **Funding:** This work is funded by the National Natural Science Foundation of China (82270692 and 81803449 to X.L.; 81603047 to Y.Y.; and 82370527 to Z.S.), the Medical Science and Technology Project of Zhejiang Province (2022488040 to X.L.), the National Key R&D Program of China (2023YFC2507400 to C.L.), the Chongqing Science Fund for Distinguished Young Scholars (CSTB2023NSCQ-JQX0021 to C.L.), and the Chongqing University Innovation Research Group (CXQT20006 to C.L.). **Author contributions:** Conceptualization: X.L., C.L., and Z.S. Methodology: Y.Y. and Y.B. Validation: B.L. and C.L. Formal analysis: Y.B. and C.S. Investigation: C.S., B.L., C.L., and L.Z. Resources: C.S., Z.S., and C.L. Data curation: Y.Y., Y.B., and X.L. Writing—original draft: Y.Y., Y.B., and C.S. Writing—review and editing: X.L., C.L., and Z.S. Visualization: L.Z. Supervision: X.L., C.L., and Z.S. Project administration: Y.Y. and Y.B. Funding acquisition: X.L., C.L., and Z.S. **Competing interests:** The authors declare that they have no competing interests. **Data and materials availability:** All data and code needed to evaluate and reproduce the results in the paper are present in the paper and/or the Supplementary Materials.

Submitted 19 June 2025
Accepted 22 October 2025
Published 2 January 2026
10.1126/sciadv.adz9069